AMS and rock magnetism in the Caviahue-Copahue Volcanic Complex (Southern Andes): Emission center, flow dynamics, and implications to the emplacement of non-welded PDCs

Mauricio Barcelos Haag [a,*], Carlos Augusto Sommer [a], Jairo Francsiso Savian [a], Alberto Tomás Caselli [b], Thiago Ribas Moncinhatto [c], Gelvam André Hartmann [d], Michael H. Ort [e], Wilbor Poletti [f], Ricardo Ivan Ferreira da Trindade [c]

[a] Instituto de Geociências, Universidade Federal do Rio Grande do Sul, Av. Bento Gonçalves 9500, 91501-970 Porto Alegre, RS, Brazil
[b] Laboratorio de Estudio y Seguimiento de Volcanes Activos, Universidad Nacional de Río Negro, Roca 1242, 8332 G. Roca, Rio Negro, Argentina
[c] Instituto de Astronomia, Geofisica e Ciências Atmosféricas, Universidade de São Paulo, Rua do Matão 1226, 05508-090 São Paulo, SP, Brazil
[d] Instituto de Geociências, Universidade Estadual de Campinas, Rua Carlos Gomes 250, 13083-855 Campinas, SP, Brazil
[e] School of Earth and Sustainability, Box 4099, Northern Arizona University, Flagstaff, AZ 86011, USA
[f] Instituto de Ciência e Tecnologia, Universidade Federal dos Vales do Jequitinhonha e Mucuri, Rodovia MGT-367, 5000, 39100-000 Diamantina, MG, Brazil

ARTICLE INFO

ABSTRACT

Pyroclastic deposits can cover significant areas and register major geological events. Despite their importance, understanding depositional dynamics of pyroclastic density currents (PDCs) and linking explosive deposits to their emission centers is still a challenge, especially in the case of non-welded, massive ignimbrites. Located in the Southern Andes, the Caviahue Copahue Volcanic Complex (CCVC) comprises one of the most active volcanic centers in the Andean Belt. This volcanic complex hosts massive ignimbrites with both source emplacement poorly constrained, currently grouped in the Riscos Bayos Ignimbrites (RBI). In this contribution, we perform a full magnetic characterization and anisotropy of magnetic susceptibility (AMS) study on the massive RBI of the CCVC. The magnetic characterization was performed using magnetic experiments including isothermal remanet magnetization, thermomagnetic curves, hysteresis loops, first-order reversal curves, and scanning electron microscopy. Magnetic experiments indicate primary, multi-domain, high Curie temperature titanomagnetites as the AMS carriers. Ellipsoids are predominately oblate, with a low degree of anisotropy and east-southeastward imbrication. This fabric arrangement is consistent with PDC sedimentary fabrics deposited under laminar flow conditions. Despite RBI massive structure AMS data reveals changes in transport capacity of the PDC and particle organization. These changes are marked by increasing AMS dispersion and decreasing degree of anisotropy up-section within flow units. Directional statistics of AMS data implies the Las Mellizas Caldera as the emission center of RBI. The reconstructed flow path also suggests the PDC overrun of the Caviahue Caldera topographic rim. This study highlights the application of AMS to the identification of emission centers of explosive deposits, featuring its application to massive ignimbrites.

© 2021 Elsevier B.V. All rights reserved.

1. Introduction

Pyroclastic density currents (PDCs) are the main products of explosive volcanism and produce a wide variety of deposits, including welded to non-welded ignimbrites (Sparks, 1976; Cas and Wright, 1987). These explosive deposits can cover extensive areas and record a significant portion of the geological history, as documented in the Snake River and Yellowstone Volcanic Province (USA; Morgan et al., 1984), Sierra Madre Occidental (Mexico; Ferrari et al., 2002), and the Altiplano-Puna Volcanic Complex (Argentina and Chile; de Silva, 1989; Lesti et al., 2011). Despite their geological significance, linking explosive deposits to their source areas and understanding depositional processes in PDCs is still a challenge, with several unresolved emission centers around the world (e.g., Morgan et al., 1984; Giordano et al., 2008; Agrò et al., 2014) and in the Andean Belt (e.g., Lesti et al., 2011; Ort et al., 2014; Platzman et al., 2020). This happens because, in active regions tectonics and climate can rapidly modify volcanic landscapes, preferentially removing non-welded deposits. As a consequence, the study of PDC deposits in these environments demands the application

* Corresponding author.
E-mail address: mauricio.haag@ufrgs.br (M.B. Haag).

of alternative techniques. The anisotropy of magnetic susceptibility (AMS) is helpful to understand the mechanisms and flow dynamics of pyroclastic flow deposits.

AMS estimates the orientation of the magnetic particles of a given rock sample, detecting a rock fabric that can be used to study paleocurrent, deformation, and rheological processes in all kinds of rocks (Graham, 1954; Hrouda, 1982; Cañón-Tapia and Mendoza-Borunda, 2014). AMS studies have been applied to volcanic rocks, allowing the determination of source area, transport, and emplacement conditions of PDCs (e.g., Palmer and MacDonald, 1999; Ort et al., 2003; LaBerge et al., 2009; Cas et al., 2011; Cañón-Tapia and Mendoza-Borunda, 2014; Ort et al., 2014), lavas (e.g., Cañón-Tapia et al., 1997; Benites et al., 2020; Pasqualon et al., 2020; Haag et al., 2021) and dikes and sills (e.g., Magee et al., 2012). Nevertheless, how PDC processes are recorded in magnetic fabrics is still debated because many factors can influence the petrofabrics to produce a variety of AMS fabrics (e.g., Ort et al., 2014; Cañón-Tapia and Mendoza-Borunda, 2014). The presence of extensive ignimbrite deposits in the Caviahue-Copahue Volcanic Complex (CCVC) in northern Patagonia provides a key area for the study of AMS fabrics in ignimbrites.

Located in the southern Andes (between Argentina and Chile), the CCVC (Fig. 1) comprises one of the most active volcanic centers in this orogenic segment (Caselli et al., 2016; Tassi et al., 2016). Despite the young age (< 5 Ma, Linares et al., 1999), CCVC deposits were strongly affected by Pleistocene glaciations (Díaz, 2003; Varekamp et al., 2006; Báez et al., 2020a), leading to a fragmented record and establishing a geologic puzzle, especially in the case of the more friable, volcaniclastic deposits. As a result, the explosive deposits in the CCVC provide an excellent case for the study of AMS fabrics in non-welded ignimbrites. The Riscos Bayos Ignimbrites (RBI), located a few kilometers outside the southern border of the Caviahue Caldera (Melnick et al., 2006), consist of a sequence of predominantly non-welded ignimbrites with restricted outcrops (Mazzoni and Licitra, 2000; Varekamp et al., 2006).

This unique low-grade ignimbrite sequence (RBI) in the region is a significant geologic unit for the understanding of the CCVC (Mazzoni and Licitra, 2000), as well as a case study for the determination of emission centers of large-volume, non-welded PDCs deposits.

This work constrains the emplacement conditions and the source area of RBI, exploring its relations with the CCVC. We conducted fieldwork at the CCVC and performed a systematic sampling for AMS analyses and full magnetic mineralogy characterization. This approach allowed us to determine the flow direction of the RBI PDCs and link the AMS with flow dynamics of these flows. Our data suggest a decrease in transport capacity toward the top of each flow unit, marked by an increase in AMS dispersion and a decrease in the degree of anisotropy. Directional analysis indicates the Las Mellizas Caldera as the emission center for the RBI.

2. Geological setting

Located in the Southern Volcanic Zone (SVZ) of the Andes (Fig. 1), the CCVC (37°50′S, 71°10′W) comprises a singular volcanic center composed of the active stratovolcano Copahue (1.23 Ma – Recent) and the Pliocene Caviahue (also known as *Agrio*) Caldera (Pesce, 1989; Melnick et al., 2006; Fig. 1). In the SVZ, the magmatic activity occurs as a result of the subduction of the Nazca Plate under the South American Plate, with extensive volcanism of basaltic to andesitic composition (Hildreth and Moorbath, 1988; Stern, 2004). In this context, the CCVC composes one of the most active volcanic centers in the Andean belt, with several eruptive events in the last century (Caselli et al., 2016; Tassi et al., 2016). The particular setting of the CCVC attracted several studies in the recent decades, with a broad range of topics including geomorphology (e.g., Díaz, 2003; Báez et al., 2020a), geochemistry (e.g., Mazzoni and Licitra, 2000; Melnick et al., 2006; Varekamp et al., 2006), geochronology (e.g., Pesce, 1989; Melnick et al., 2006) structural (e.g., Melnick et al., 2006; Velez et al., 2011; Folguera et al., 2016),
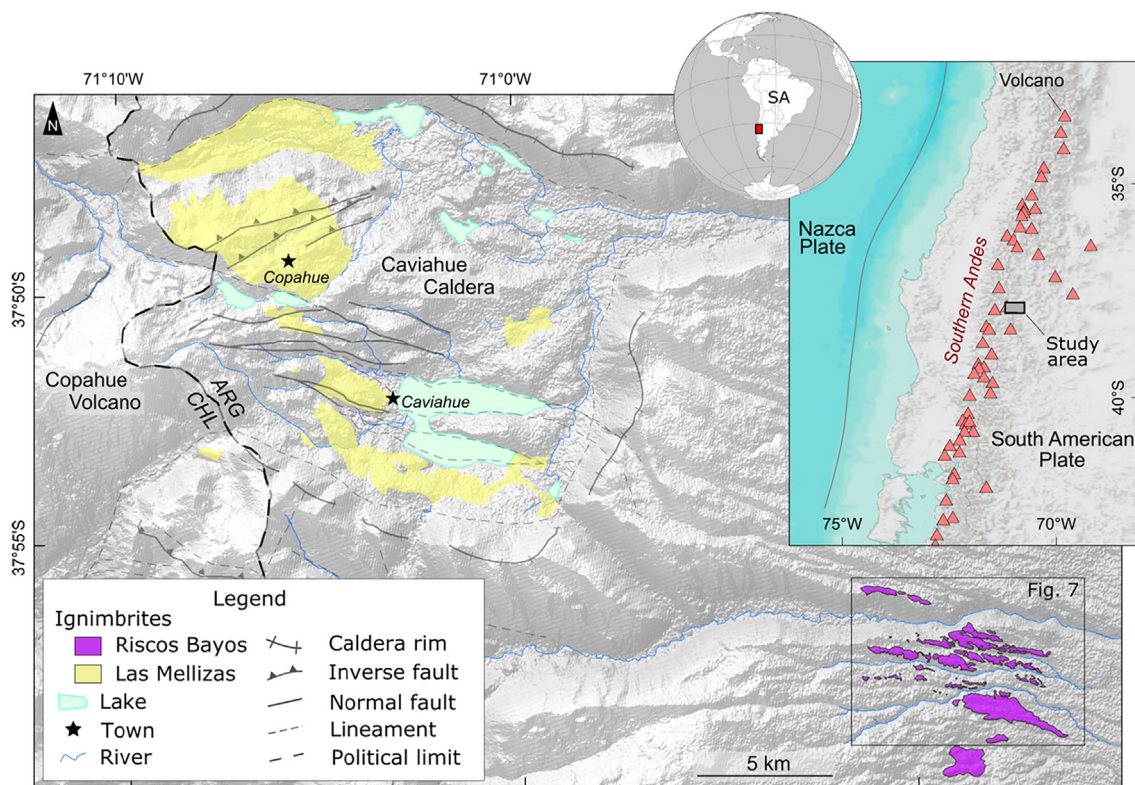

Fig. 1. Shaded relief map of the CCVC with the main ignimbrite deposits, geological features, and structures. ARG - Argentina; CHL - Chile. To the right: inset with the context of the studied area in the globe and in the Southern Andean Belt. SA - South America.

geothermal (e.g., Barcelona et al., 2019), and AMS and paleomagnetism (e.g., Ort et al., 2014; Moncinhatto et al., 2019, 2020).

Both Copahue and Caviahue are controlled by a complex structural setting, with significant influence of the oblique subduction of the Nazca Plate on caldera and volcano edifice morphology (Melnick et al., 2006), as well as on vent location and spatial distribution (Stern, 2004; Sielfeld et al., 2017). In addition to this active tectonic setting, several features indicate a strong glacial imprint on CCVC deposits, including U-shaped valleys, striations in lava flows, and moraine deposits (Díaz, 2003; Varekamp et al., 2006; Báez et al., 2020a). The age and intensity of this glaciation are still unclear (Báez et al., 2020a).

The CCVC is marked by abundant effusive and explosive deposits (Melnick et al., 2006), which extensively cover and partially fill the Caviahue Caldera. Related to Pleistocene evolution, two main pyroclastic units are identified in the region (Mazzoni and Licitra, 2000): the Las Mellizas Volcanic Sequence (LMVS, ~ 2.6 Ma; Linares et al., 1999), which occupies the inner portion of the Caviahue Caldera, and the Riscos Bayos Ignimbrites (RBI, 2.0–1.1 Ma; Muñoz and Stern, 1988; Linares et al., 1999), which are prominently located about 15 km southeast of the Caviahue Caldera but also cover ~100 km^2 on the top of the mesa to the east of the caldera (Fig. 1). The LMVS is marked by strongly welded andesitic to dacitic ignimbrites and rheoignimbrites containing abundant lithic fragments (Mazzoni and Licitra, 2000; Melnick et al., 2006; Sommer et al., 2016), interbedded with extensive lava flows (Varekamp et al., 2006).

In contrast, the RBI forms irregular ENE-WSW-trending ridges (Fig. 1) in the Riscos Bayos area and consists of a sequence of predominantly non-welded rhyolitic ignimbrites, with an abundant ash matrix composed of pumice and lithic fragments of volcanic origin (Mazzoni and Licitra, 2000; Melnick et al., 2006; Varekamp et al., 2006). On the mesa to the east of the Caviahue caldera, the ignimbrite, up to ~100 m thick, is incipiently to moderately welded and forms ENE-WSW-trending ridges. Additional mapping of RBI is still necessary to determine the total extent of the deposits (Ort et al., 2014). The available data indicate contrasting ages for RBI, caused either by analytical errors or contamination (Melnick et al., 2006).

Both vent location and nature of the RBI are also poorly constrained. Some studies have associated this ignimbrite sequence with the collapse of the Las Mellizas Caldera (Pesce, 1989; Melnick et al., 2006), a volcano originally located to the west of the Caviahue Caldera where the Copahue Volcano is now located. Others associate RBI with Caviahue Caldera collapse (Mazzoni and Licitra, 2000), while some authors have argued that RBI could not account for the collapse based on volume estimates (Varekamp et al., 2006). These volume estimates, in contrast, are still debated (Ort et al., 2014).

3. Methods

3.1. Fieldwork and paleomagnetic sampling

RBI outcrops were first identified using Google Earth and available geological maps from the literature (e.g., Melnick et al., 2006). The best accessible RBI exposures occur 15 km SW of the southeastern rim of the Caviahue Caldera, along the Argentinian road number 26. A field evaluation regarding the main structures and primary constituents was performed in every outcrop, including compass measurements. For AMS studies, a total of 144 cores (25.4 mm in diameter) were obtained from 10 sampling sites using a portable gasoline-powered drill. The samples were oriented using a magnetic compass and whenever possible a sun compass for corrections.

3.2. Laboratory investigations

3.2.1. Microscopy

Thin sections were prepared and analyzed under an optical microscope with transmitted (for silicate fabrics) and reflected light

(for Fe—Ti oxide fabrics). Using the software ImageJ (Schindelin et al., 2012), the orientation of the major axis of both silicate and oxide crystals of representative samples were extracted, allowing comparison and validation of the directions obtained using the AMS technique.

3.2.2. Rock magnetism

To identify the magnetic carriers and the nature of the magnetism in RBI, we characterized our samples using several experiments including temperature-dependent magnetic susceptibility curves (χ-T), isothermal remanent magnetization (IRM) acquisition curves, hysteresis loops, and first-order reversal curves (FORC). All magnetic measurements were performed at the Paleomagnetism Laboratory of the University of São Paulo (USPMag).

One representative powdered sample from each site (total of 10 samples) was used to determine the Curie temperature (Tc) and phase transitions and of the magnetic minerals using temperature-dependent low-field magnetic susceptibility curves (χ-T diagrams). The samples were heated from room temperature up to ~600 °C using a Kappabridge KLY4 coupled with a CS3 furnace (AGICO). The results were corrected and analyzed using the software Cureval8 (AGICO), where the Tc values were obtained by the second derivative of the heating curve (Tauxe et al., 2018).

IRM curves and hysteresis loops were determined using small rock chips from each site. Analyses were performed at room temperature using a Princeton Measurements Corporation Micromag vibrating sample magnetometer (VSM) by applying fields up to 1 T. From these analyses, we derived basic parameters, including the saturation magnetization (Ms), saturation remanent magnetization (Mrs), coercivity (Bc), and coercivity of remanence (Bcr). In order to model the magnetic components present in our samples, UnMix analyses (Robertson and France, 1994; Kruiver and Passier, 2001; Heslop et al., 2002) were performed using the IRM acquisition curves. Quantification and UnMix fitting were accomplished using the MAX UnMix application (Maxbauer et al., 2016), with a smoothing factor of 0.5.

Hysteresis parameters are not sufficient for discriminating the different magnetic components and structural states because they provide only a measurement of the sample bulk properties (Roberts et al., 2018). Considering the complex magnetic mineralogy observed in our samples (Moncinhatto et al., 2020), we obtained FORCs to better characterize our magnetic assemblage. FORC diagrams (Roberts et al., 2000) were obtained at room temperature after 300 reversal curves with an average time of 200 ms. The data were processed using the FORCinel software package (Harrison and Feinberg, 2008), applying a smoothing factor of 5 to all samples.

Further investigation of silicate and iron oxide composition was carried out using a scanning electron microscope (SEM) model Jeol JSM 6610-LV operated at a beam voltage of 15 kV, and energy-dispersive X-ray spectroscopy (EDS), at the Laboratory of Isotope Geology of the Federal University of Rio Grande do Sul (LGI-UFRGS).

3.2.3. AMS analysis

In this work, we apply the AMS to interpret the petrofabrics of the studied ignimbrites and determine the flow direction of the PDC. The AMS signal consists of a superposition of diamagnetic, paramagnetic and ferromagnetic minerals, depending on their intrinsic anisotropy and spatial distribution within a rock sample (Tarling and Hrouda, 1993). This technique is based on the measurement of the magnetic susceptibility in different directions to resolve the magnetic susceptibility tensor (K), which ultimately represents the shape and orientation of the particles in the sample (represented by the principal axes $K_1 \geq K_2 \geq K_3$), allowing several interpretations related to flow direction and regime in volcanic rocks (Graham, 1954; Cañón-Tapia and Mendoza-Borunda, 2014).

In the laboratory, samples were cut into standard specimens (25.4 mm in diameter, 22 mm in thickness), totaling 144 specimens. AMS analyses were performed on standard specimens from all sites,

using an automatic Kappabridge MFK1-A apparatus (AGICO), operated in a low alternating field of 300 A/m and a frequency of 976 Hz. Results were processed and interpreted using Anisoft5 (AGICO), and later plotted in a geographic information system (GIS) environment to aid the spatial interpretation. All the stereonets presented are in the bedding coordinate system (bedding being rotated to the horizontal).

All AMS analyses were performed at the USPMag. To reach a more robust directional analysis, we also reprocessed 13 paleomagnetic sites from Ort et al. (2014), who performed an AMS and paleomagnetic analysis in the CCVC with a greater focus on AMS fabrics and their behavior with respect to PDC deposition. In order to better constrain confidence intervals and the principal AMS axes, bootstrap resampling was applied to our samples (Constable and Tauxe, 1990; Tauxe et al., 1991).

4. Results

4.1. Field and petrographic aspects

In the study area the RBI crops out as ENE-WSW-trending ridges marked by distinct tan, white and grey colors (Fig. 2A). The northern section is dominated by tan and grey irregular ridges stretching for up to ~3 km, while the southern section is composed of a white ~4-km-long continuous ridge. Flow units are tabular, with thickness ranging from a few to 15 m (Fig. 2B). RBI samples are mainly poorly sorted lapilli-tuffs with 20 to 35% of ash, 65 to 75% of lapilli, and less than 2% of block fragments. The lapilli and block fragments are mainly composed pumice (80–95%) fragments, with variable contents of lithic
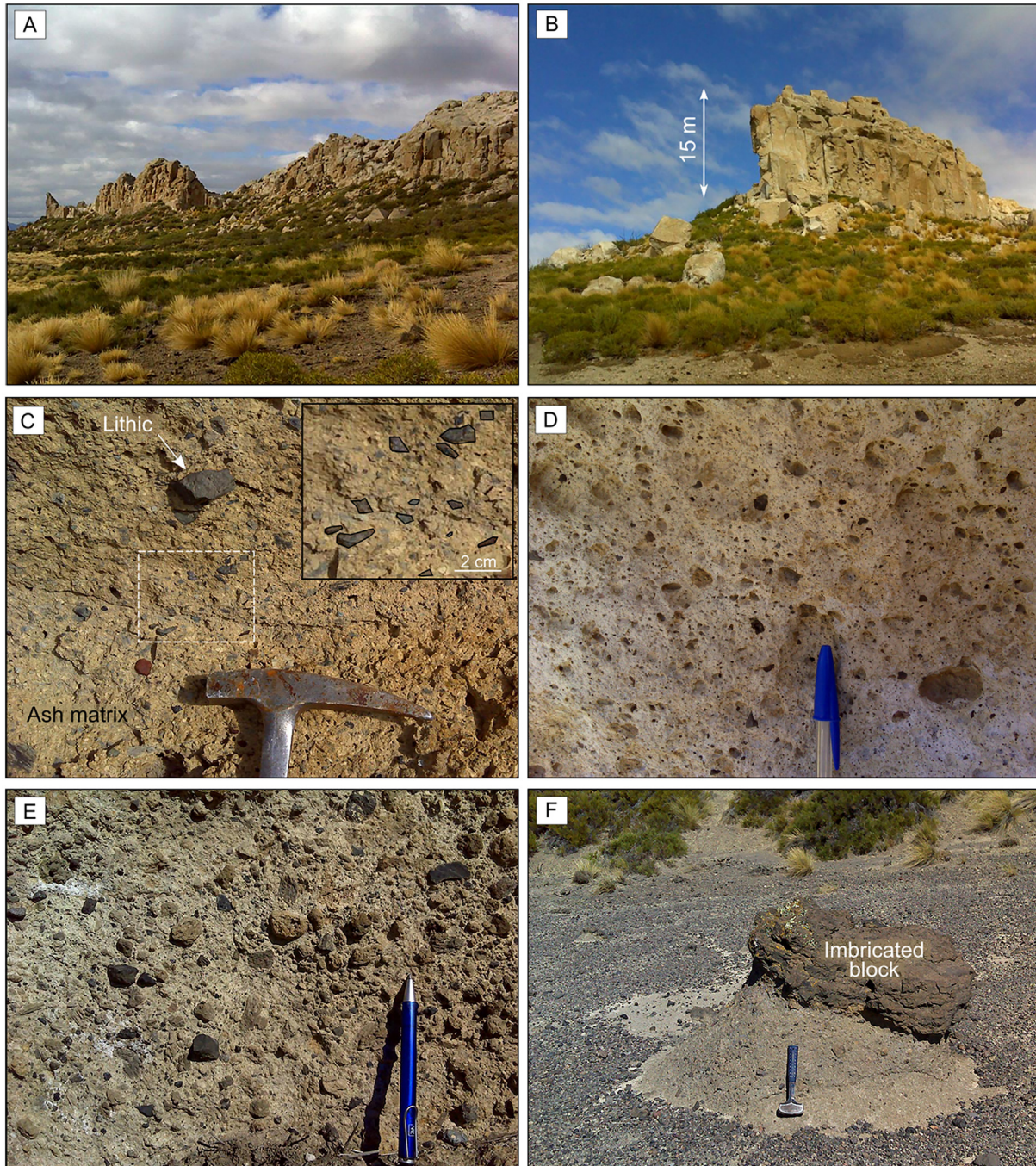

Fig. 2. Field and petrographic aspects of RBI. A) ENE-WSW-trending ridges of RBI outcrops; B) outcrop of tan-colored ignimbrite sequence; C) poorly-sorted lapilli-tuff with incipient imbrication (inset); D) upper section pumiceous lapilli-tuff; E) lithic-rich basal section; F) block-sized imbricated fragment.
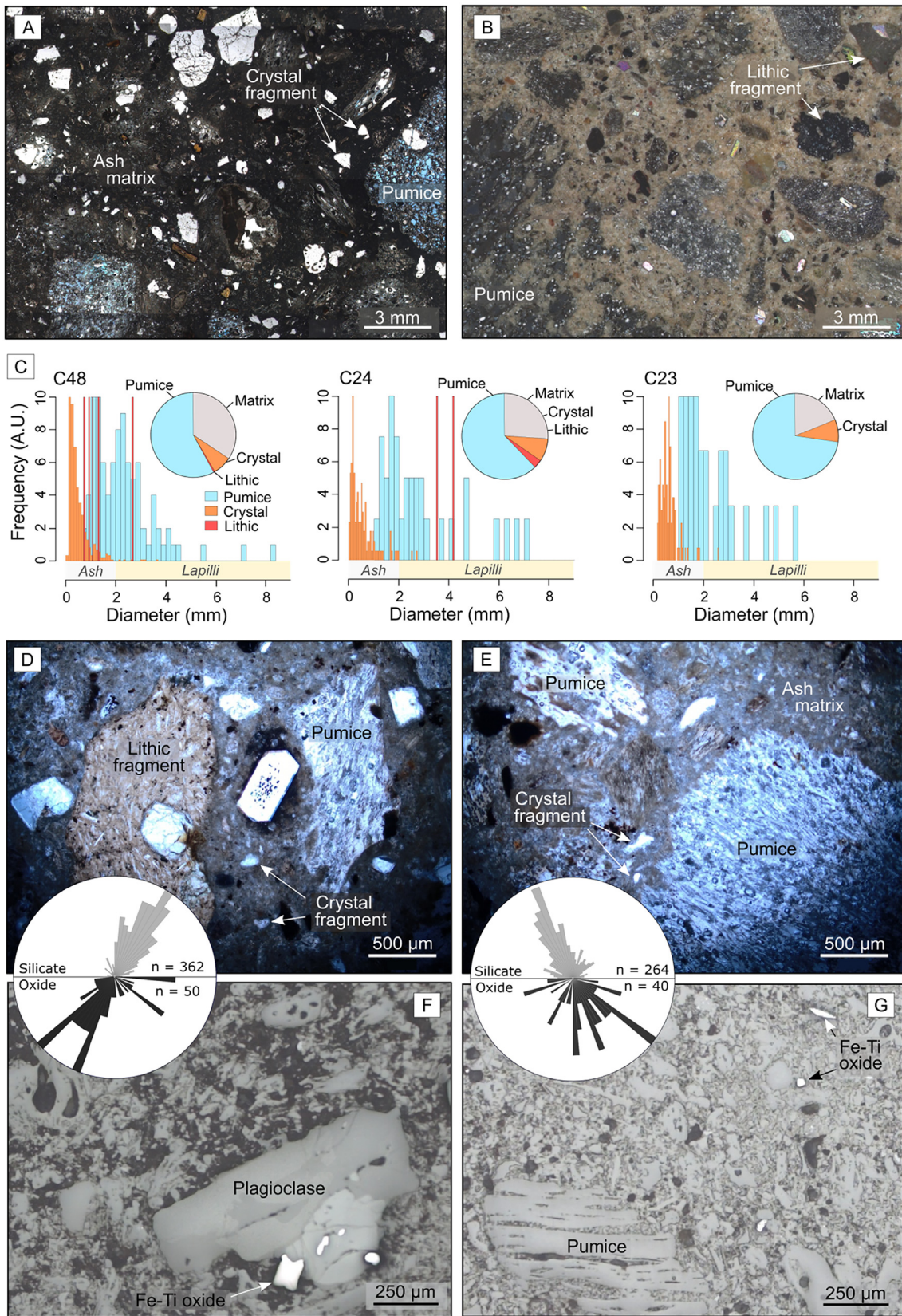
Fig. 3. Petrographic aspects of RBI. A) lapilli-tuff rich in crystals (transmitted light); B) lapilli-tuff rich in pumice and lithic fragments (transmitted light); C) compositional estimates and size distribution of pumice, crystal, lithic and matrix of RBI main body. D) lapilli-tuff showing volcanic lithic, pumice, and crystal fragments (transmitted light); E) lapilli-tuff rich in non-welded pumice fragment and ash matrix (transmitted light); F) detail of plagioclase crystal and several Fe—Ti oxides (reflected light); G) detail of ash matrix, pumice fragment, and Fe—Ti oxide crystals (reflected light). Rose diagrams indicating both oxide and silicates (plagioclase crystals and pumice fragments) major axis orientation;

clasts (5–20%), mainly of andesite and basalt (Fig. 2C, D). Pumice, lithic and crystal are supported by a fine matrix mainly composed of pumice and crystal fragments.

In some sites, the matrix and the clasts present a slight imbrication to the southeast (Fig. 2C). Despite that, massive and graded bedding dominates as the main structures observed in RBI. A normal grading for lithic clasts and an inverse grading for pumice clasts are common, as well as pumice concentration zones. The upper section presents high primary and secondary porosities and is marked by higher pumice contents (Fig. 2D). Pumice fragments can reach up to 20 cm in diameter. In the basal section, thin horizons with a concentration of lithic clasts are common (Fig. 2E), where lithic fragments can reach up to 30 cm in diameter. In several locations, a high variation in grain size and distribution occurs, including the sparse presence of blocks and bombs (Fig. 2F).

Under the microscope, RBI samples are marked by pumice, lithic, and crystal fragments surrounded by fine ash matrix. The ash matrix is predominantly composed of partially oxidized shards, as well as crystal fragments (Fig. 3A, B). Crystal, lithic and pumice fragments are typically lapilli, with diameters ranging from 3 to 30 mm (Fig. 3A-D). Petrographic compositional estimations of RBI main body (Fig. 3C) reveal a predominance of pumice fragments (66–90%), followed by crystal (4–9%) and lithic fragments (1–3%). Pumices dominate the lapilli and ash size intervals, while crystals tend to concentrate within the ash fraction (Fig. 3C). The amount of matrix ranges from 15 to 40%.

Quartz and feldspar dominate as the main crystal fragments, which are marked by sharp and irregular shapes (Fig. 3A, B, D, E). Volcanic rocks (basaltic to basaltic-andesite in composition) predominate as the main lithic clasts, tipically unaltered, with irregular to slightly rounded shapes (Fig. 3B, D). Pumice fragments are marked by irregular shapes and high porosity values, without signs of welding or viscous/ductile deformation (Fig. 3A - porosity in blue, D, E).

Reflected light microscopy reveals the presence of a small, sparse, distribution of Fe—Ti oxides in RBI samples (Fig. 3F-G). These crystals commonly occur as primary crystals, adjacent to the silicate fabric (Fig. 3F), or as crystal fragments disseminated in the ash matrix (Fig. 3G). Fe—Ti oxides in the RBI commonly present diameters <200 μm and are marked by small differences between their major and minor axis, defining a shape anisotropy. Using the software ImageJ (Schindelin et al., 2012), we measured the orientation of the major axis of both silicate and Fe—Ti oxide particles. The results indicate that major axes of both silicates and oxides present similar, almost parallel orientation (rose diagrams in Fig. 3).

4.2. Rock magnetism

Measurements of χ-T curves were carried out in one sample from each site (Table 1) to assist the determination of the magnetic phases, their structure, and alteration history (e.g., Tarling and Hrouda, 1993; Hrouda, 2003). RBI samples present a variety of thermomagnetic curves (Fig. 4A-C), with two main sets of transition temperatures (T). All samples

are marked by a high transition temperature (T_1), ranging from 472 to 580 °C (Fig. 4A, B, C). In addition to the T_1, some samples present a secondary low transition temperature (T_2), ranging from 279 to 410 °C (Fig. 4B, C). When compared, heating and cooling cycles display minor differences (Fig. 4A, B, C), with small values of the A_{40} and A_{MAX} indices (Hrouda, 2003), suggesting that the susceptibility is mostly reversible and new magnetic phases were not created during the experiment.

Hysteresis loops commonly display a narrow hysteresis, with coercivities <24 mT (Table 1) and low slopes, suggesting small contents of paramagnetic minerals (Fig. 4D). IRM acquisition curves show that all samples reach saturation with fields ranging from 200 to 400 mT (Fig. 4E; Table 1), which indicates the dominance of low-coercivity magnetic minerals, such as magnetite, maghemite, and greigite, which usually present Ms. <300 mT (Dunlop and Özdemir, 1997). However, several samples (Fig. 4E) are not completely saturated at 300 mT, which indicates a small concentration of high-coercivity minerals such as hematite and goethite. Hysteresis data, including the ratio of saturation remanence to saturation magnetization (M_{rs}/M_s) and the coercivity of remanence to coercive force (H_{cr}/H_c), can be used in the Day plot, a diagram that can help discriminate between single domain (SD), pseudo-single domain (PSD) and multidomain (MD) particles (Day et al., 1977). This differentiation is important because it can have effects on the behavior of the magnetic particles (e.g., Moncinhatto et al., 2020). The RBI samples (Table 1) lie within the pseudo- PSD and MD of the Day plot (Fig. 4F, Day et al., 1977).

UnMix processing reveals three distinct components contributing to the magnetization observed in RBI samples (Fig. 4G, H, I). Overall, samples are characterized by either a single component or two components (Table 1). Component 1 (B_1) is observed in all samples and provides the strongest contribution to net magnetization (81,2 to 100%), with average field ranges from 37.3 to 73.41 mT (Fig. 4G, H, I; Table 1). A second component (B_2) is also observed in some samples, with fields ranging from 149.8 to 352.4 mT and contributions of less than 18.7% to the net magnetization (Fig. 4H; Table 1). A third component (B_3) was detected in only one sample (Fig. 4I; Table 1 - sample C29). B_3 displays the lowest coercivity among our samples (9.3 mT), with a contribution to the net magnetization of 15.9% on sample C29.

FORC diagrams typically display two components (Fig. 4J, K, L), where the first is marked by a spread along the field distribution (Bu) axis and low coercivity (Bc) values and the second is marked by Bu values centered around zero and a spread along the Bc axis. The first behavior of FORC distribution is compatible with MD behavior, while the second indicates the presence of samples with vortex domain structure (Roberts et al., 2000, 2017, 2018). Please check supplementary items 1, 2, and 3 for a full report on the magnetic experiments.

4.3. SEM observations

SEM observations and compositional maps obtained using EDS mapping reveal titanomagnetite crystals with variable amounts of Ti as the main oxides present in RBI samples (Fig. 5). These crystals occur

Table 1
Summary of magnetic mineralogy in RBI samples.

Unit	Site	Hysteresis and IRM results						χ-T curves	UnMix processing	FORC
		M_s (mAm²/Kg)	M_{rs} (mAm²/Kg)	H_c (mT)	H_{cr} (mT)	H_{cr}/H_c	M_{rs}/M_s	Transitions (°C)	Components (mT)	behavior
RB1	COP23	566.9	158.0	23.8	60.0	2.52	0.28	603	62.2 (B_1), 352.4 (B_2)	SV
RB2	COP24	322.2	45.1	10.9	40.4	3.71	0.14	472	42.7 (B_1), 149.8 (B_2)	MD
RB3	COP25	824.5	126.8	20.0	54.3	2.72	0.15	580, 410	70.1 (B_1)	MD + SV
RB1	COP26	240.5	38.6	11.8	37.0	3.13	0.16	499, 279	37.3 (B_1), 207.2 (B_2)	MD + SV
RB2	COP27	1034.1	144.3	15.4	35.8	2.33	0.14	567	46.1 (B_1)	MD
RB2	COP29	423.9	32.66	6.2	30.5	4.87	0.08	535	50.2 (B_1), 9.63 (B_3)	MD
RB2	COP30	420.9	86.73	17.6	37.3	2.12	0.21	537	50.5 (B_1)	MD
RB2	COP31	411.45	43.58	8.4	36.9	4.38	0.11	573, 299	45.3 (B_1)	MD
RB3	COP48	395.4	84.2	22.8	58.3	2.55	0.21	647, 579	73.4 (B_1)	–
RB3	COP49	862.4	70.4	9.9	40.3	4.07	0.08	646, 577, 484	55.6 (B_1)	–

Symbols: FORC states: MD = multi-domain; SV = single-vortex (Roberts et al., 2000, 2017, 2018).
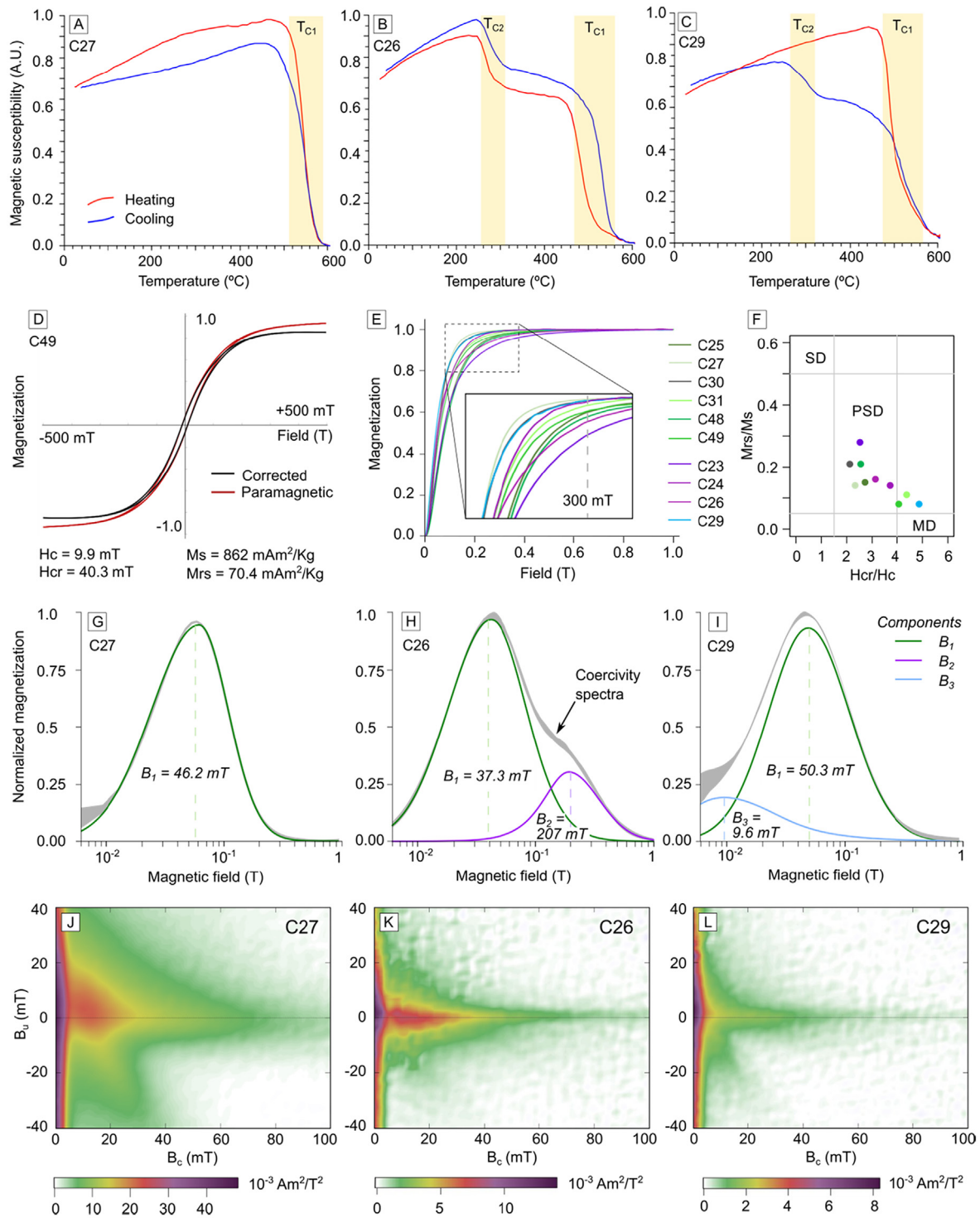
Fig. 4. Summary of magnetic experiments: A–C) χ-T curves; D) representative hysteresis loop; E) IRM curves from all sites; F) Day plot (Day et al., 1977), site colors are the same as E; G- I) representative coercivity spectra and UnMix fitting; J-L) representative FORC diagrams. A.U. = Arbitrary Units.

especially as free crystals scattered in the ash matrix (Fig. 5A, B, C), as well as inclusions in pumice fragments (Fig. 5B) and silicate crystals (Fig. 5C, D). Minute ferromagnetic crystals are also present in the crystallographic structure of silicate minerals (Fig. 5D). Lithic fragments containing embedded titanomagnetite crystals are also observed (Fig. 5E, F), suggesting some contribution of non-primary magnetic phases to the observed magnetization and possible nature of the AMS signal.

The observed titanomagnetite grains display a wide variation in grain size, distribution, and shape, with a predominance of irregular crystals with diameters ranging from ~10 to 200 μm (Fig. 5). EDS spectra and compositional mapping reveal a predominance of low-Ti titanomagnetite (Ti contents ranging from 9 to 18%), although a second population of high-Ti titanomagnetite (Ti contents up to 50%) is also observed in a few samples (Fig. 5C, sample C23).
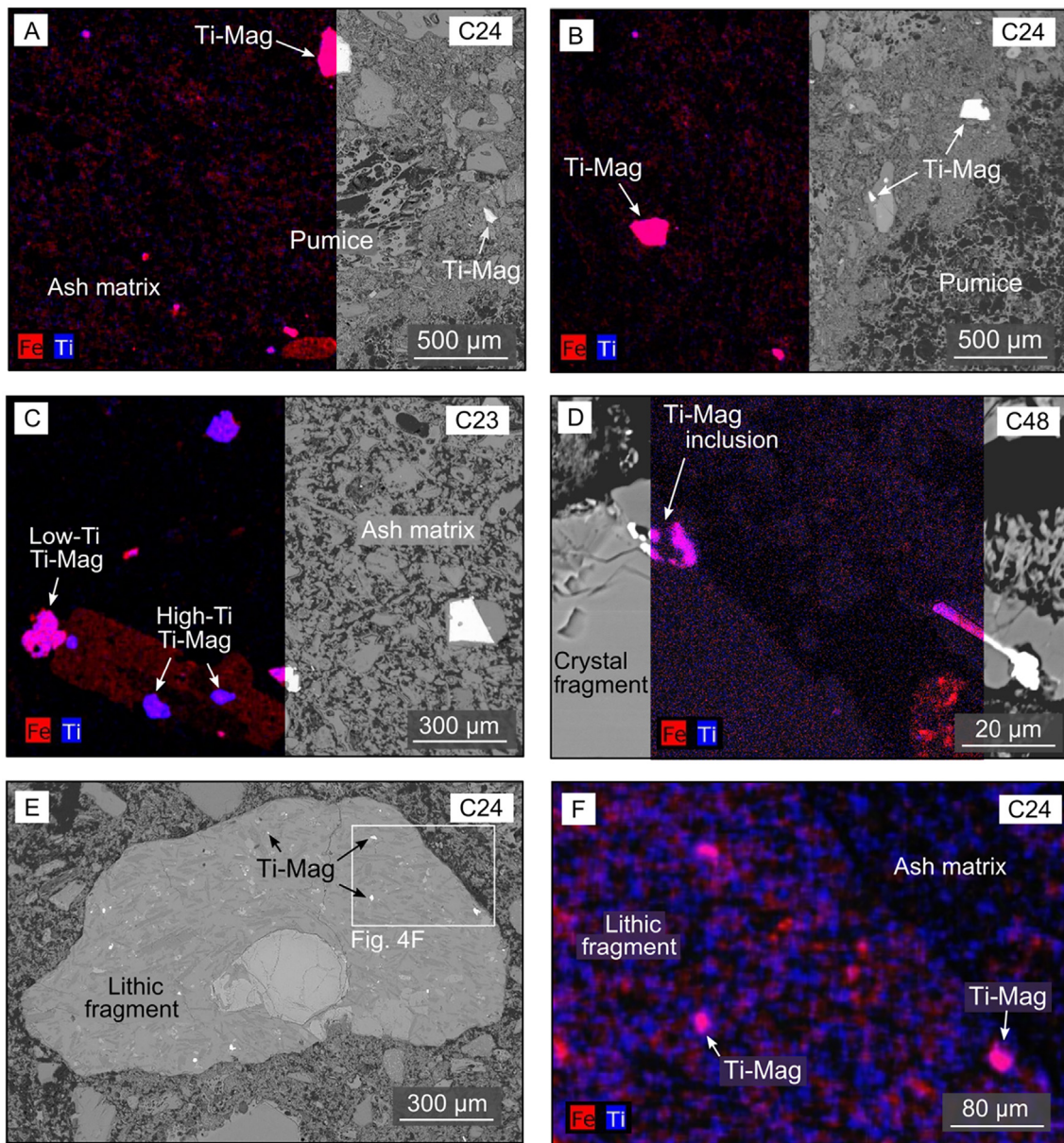
Fig. 5. SEM observations of RBI, compositional maps (dark colour), and backscattered images (greyscale images). A) titanomagnetite crystals (~200 μm) scattered in the ash matrix; B) titanomagnetite crystals (~100 μm) embedded in pumice fragment; C) titanomagnetite crystals with two distinct Ti contents and sizes (~50 to 150 μm) as inclusion in the silicate fabrics (left) and free crystals (right); D) minute titanomagnetite crystals (~10 μm) as inclusions in the crystallographic structure of silicate minerals; E) lithic fragment of andesitic compositions with several embedded Fe–Ti oxides; F) zoom in Fig. 5E, revealing disperse titanomagnetite crystals in the lithic fragment.

Table 2
AMS results for the studied sites.

Site	UTM coordinates		Scalar results					Directional results					
	mE	mN	Km (10^{-3} SI)	L	F	P′	T	K_1 D (error)	K_1 I (error)	K_2 D (error)	K_2 I (error)	K_3 D (error)	K_3 I (error)
C23	341,846	5,797,060	7.00	1.003	1.010	1.014	0.462	065 (25)	02 (08)	334 (25)	11 (07)	164 (09)	78 (07)
C24	341,846	5,797,060	3.52	1.005	1.004	1.010	−0.127	337 (27)	63 (23)	186 (14)	23 (25)	091 (41)	11 (22)
C25	343,248	5,797,194	3.25	1.010	1.019	1.031	0.328	299 (20)	19 (08)	208 (21)	02 (11)	112 (13)	70 (08)
C26	342,200	5,797,020	2.46	1.004	1.005	1.010	0.085	310 (57)	44 (21)	216 (57)	03 (31)	123 (33)	45 (21)
C27	342,191	5,796,983	6.50	1.005	1.006	1.012	0.125	297 (42)	28 (23)	201 (43)	11 (24)	092 (44)	59 (25)
C29	339,110	5,797,170	4.16	1.009	1.011	1.020	0.118	312 (09)	27 (06)	221 (12)	03 (07)	124 (13)	62 (06)
C30	339,107	5,797,178	3.41	1.003	1.004	1.007	0.188	310 (14)	17 (06)	042 (17)	07 (13)	154 (16)	71 (05)
C31	339,174	5,797,067	2.97	1.010	1.008	1.018	−0.047	277 (33)	21 (12)	009 (32)	03 (17)	106 (33)	69 (10)
C48	344,246	5,794,139	3.86	1.012	1.020	1.033	0.254	279 (12)	21 (21)	010 (25)	02 (10)	106 (13)	68 (11)
C49	342,706	5,795,376	3.56	1.011	1.022	1.035	0.320	318 (17)	22 (10)	050 (21)	05 (10)	152 (16)	67 (10)

Key: number of samples (n), average magnetic susceptibility (km), lineation (L), foliation (F), degree of anisotropy (P′), shape parameter (T; Jelinek, 1981).

4.4. AMS and structural data

A total of 144 specimens were analyzed, in addition to the 145 specimens previously analyzed by Ort et al. (2014), representing a total of 23 AMS sites (total of 289 specimens). A summary of both scalar and directional data is presented in Table 2. RBI samples present a low mean magnetic susceptibility (K_m), with most values clustering below 10×10^{-3} SI (Fig. 6A). Notably, some sites from Ort et al. (2014) present high K_m values (Fig. 6A, sites O22, 25, and 26), which is associated with the increased welding degree of these sites on the mesa east of Caviahue caldera.
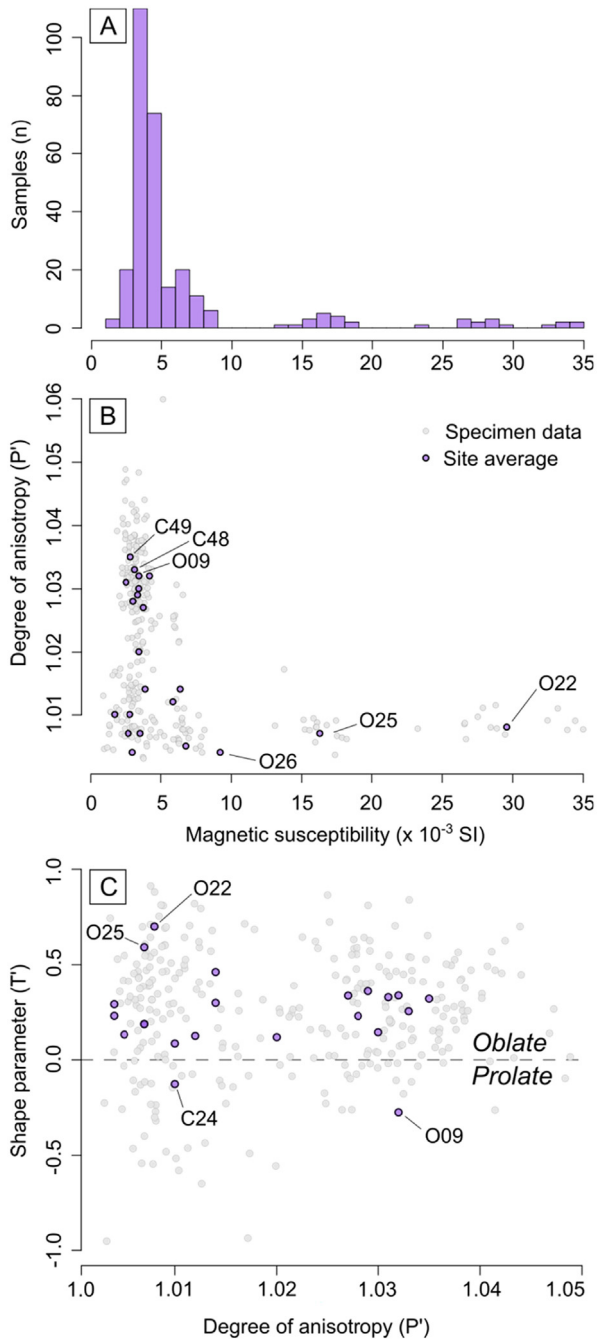
Fig. 6. Summary of AMS scalar results: A) distribution of the bulk magnetic susceptibility; B) degree of anisotropy and the bulk magnetic susceptibility; C) shape parameter and degree of anisotropy.

Samples present a low degree of anisotropy (P′), with typical values ranging from 1.003 to 1.05 (Fig. 6B). The higher P′ values are observed in samples C48, C49, and O09, notable sites with low Km values and variable T parameters (Fig. 6B, Table 2). The shape parameter (T) of magnetic tensors indicates a predominance of oblate ellipsoids, although some samples may fall within the prolate and triaxial fields (Fig. 6C). Only two sites present prolate tensors (Fig. 6C, C24, and O09).

In order to assist the structural analysis, the AMS directional data were plotted in a detailed map along with representative geological structures (Fig. 7). The magnetic axes within each AMS site are typically well grouped (with the exception of sites C24 and C27 in Fig. 7), allowing AMS-based interpretations (Table 2). In most sites, the K_3 presents a general east to southeast plunge, and the magnetic lineation (K_1) is parallel to this direction, with a few exceptions (e.g., site C23, C24, C26, C27, and O09 in Fig. 7). In several sites, both K_1 (magnetic lineation) and K_2 tend to clusters (e.g., C26 and O26), suggesting the presence of oblate ellipsoids, with a well-defined K_3 (pole of the magnetic foliation).

5. Discussion

To identify the source area and volcanological processes associated with the RBI, we integrate fieldwork, AMS, and detailed magnetic mineralogy investigations. In the following sections, we discuss the origin of the magnetic anisotropy, the emplacement dynamics and source area of RBI, and its implications for the CCVC evolution. Finally, we compare our results with available AMS data from pyroclastic sequences, addressing some of the questions related to PDC dynamics and emplacement.

5.1. Origin of the magnetic petrofabrics

Recent studies have shown that AMS fabric of pyroclastic materials is strongly dependent on microscopic factors, such as composition, mineral magnetic interactions, and domain structure of the Fe—Ti oxides (e.g., Cañón-Tapia and Mendoza-Borunda, 2014; Moncinhatto et al., 2020). The AMS in pyroclastic deposits results from four main sources (Cañón-Tapia and Mendoza-Borunda, 2014): (1) ferromagnetic phases (mainly Fe—Ti oxides) present as free crystals, (2) ferromagnetic crystals embedded in the ash matrix, pumice, clasts or shards, (3) paramagnetic minerals and (4) ferromagnetic phases as inclusions on the crystallographic structure of ferrosilicate crystals. Our samples present K_m values in the range of 10^{-3} SI, and according to Tarling and Hrouda (1993) K_m values $>10^{-2}$ SI imply an AMS dominated by the ferromagnetic phases, while $K_m < 10^{-4}$ SI suggest an AMS dominated by paramagnetic minerals. The theoretical contribution of paramagnetic minerals to K_m (K_{PARA}) can be estimated using the geochemical composition of RBI and the equations of Syono (1960) and Rochette et al. (1992):

$$K_{PARA} = -14.6 + d\left(25.2\,Fe^{+2} + 33.4\,Fe^{+3} + 33.8\,Mn^{+2}\right) \text{ in } 10^{-6}\,SI$$

where d is the density of rock (assumed 2.3 g/cm³) and Fe^{+2}, Fe^{+3}, and Mn^{+2} are atomic weight percent. For the estimate, we used 16 whole-rock geochemical analyses available in the literature (Mazzoni and Licitra, 2000; Varekamp et al., 2006). On average, K_{PARA} ranges from 2×10^{-10} to 1.4×10^{-9} SI, revealing an insignificant paramagnetic contribution to K_m and suggesting a main ferromagnetic origin for the AMS in our samples.

Petrographic analyses indicate the existence of shape anisotropy in the Fe—Ti oxides. These crystals occur mainly as sparse, inequant crystals in the ash matrix (Fig. 3). Directional analysis reveals that both-silicate and Fe—Ti oxides present similar orientation (Fig. 3, rose diagrams), indicating an effective orientation of both magnetic and silicate fabrics (Archanjo and Launeau, 2004; Bascou et al., 2005). Considering the sparse occurrence of Fe—Ti oxides and absence of clusters, the effects of distribution anisotropy (i.e., the anisotropy resulting
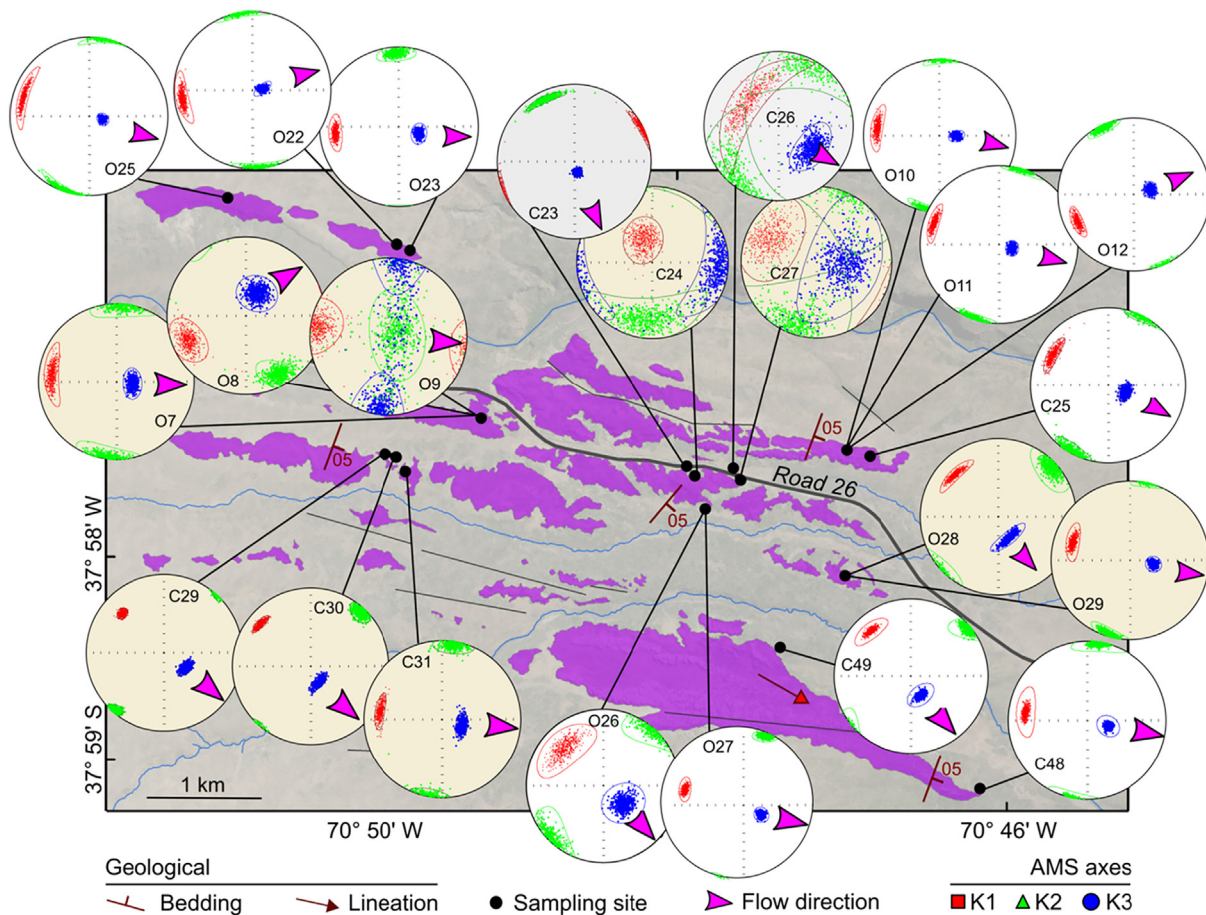
Fig. 7. Geological map of RBI, obtained bootstrapped AMS results, and inferred flow directions.

from clusters of magnetic particles; Hargraves et al., 1991) seems to be negligible in our samples. In this context, the resulting magnetic fabrics in RBI are dominated by the shape anisotropy of the ferromagnetic phases (Cañón-Tapia, 2001).

Thermomagnetic curves indicate the presence of three magnetic phases: low-Ti titanomagnetite (T₁, Lattard et al., 2006), high-Ti titanomagnetite, and possibly maghemite (T₂, e.g., Dedzo et al., 2011; Lattard et al., 2006). While T_1 is observed in all samples, T_2 is observed in only half of our dataset. These observations are confirmed by both hysteresis and IRM curves, which point to the predominance of soft magnetic phases with low Hc values grouped in three distinct coercivity components: B_1 (Hc = 37,3 to 73,41 mT), compatible with magnetite, B_2 (Hc = 149,8 to 352,4 mT), compatible with hematite and B_3 (Hc = 9.3 mT) compatible with magnetite with larger grain-size when compared to B_1 or maghemite (Roberts et al., 1995; Dunlop and Özdemir, 2015).

In all cases, titanomagnetite grains were the dominant phase detected in SEM observations, suggesting a minor contribution of secondary magnetic phases (i.e., maghemite). As a consequence, the variable presence and proportion of coercivity components may be associated with lithological heterogeneities observed in the RBI, as the Fe—Ti oxides embedded in lithic fragments revealed by SEM observations (Fig. 5E, F). Based on the uniform magnetic mineralogy of the studied samples, changes in the AMS fabrics of RBI are linked to flow dynamics.

5.2. Flow dynamics and emission area

The predominance of imbricated oblate fabrics in our samples suggests a sedimentary-related fabric as the main fabric recorded in the

RBI, resulting from the deposition and alignment of inequant ferromagnetic particles in the PDC (Cañón-Tapia and Mendoza-Borunda, 2014). Similar to granular flow in sedimentary systems, the K_1 in sedimentary fabrics of PDCs is imbricated and parallel to the flow direction (e.g., Ort, 1993; Cañón-Tapia and Mendoza-Borunda, 2014; Alva-Valdivia et al., 2017). In contrast, the development of shear and post-emplacement fabrics (e.g., slumping, compaction) seems absent in our samples, because the sampled RBI units are predominantly non-welded (Mazzoni and Licitra, 2000; Melnick et al., 2006) and present emplacement temperature below the minimum welding temperature (Haag et al., 2020).

At a site scale, AMS ellipsoids are generally well defined (Fig. 7, Table 2), with well-grouped axes and consistent ESE K_3 imbrication, suggesting nearly stable deposition dynamics (Cañón-Tapia and Mendoza-Borunda, 2014). In contrast, a few sites present large confidence ellipses and dispersion (e.g., sites C24, 26, 27, and O09 in Fig. 7), which may be linked to either poorly defined AMS tensors (low P′) or unsteady depositional dynamics (Cañón-Tapia and Mendoza-Borunda, 2014).

When considering a more regional scale (up to a few hundred meters), AMS sites reveal slight variations in the PDC direction. This is highlighted by several groups of proximal sites (e.g., group C30, 31 and group O7, 8, 9) that, despite having sites located just a few meters from each other, present significant directional deviations (up to 33° in K_1 direction in group O7, 8, 9) in the resulting AMS tensor (Fig. 7). Despite these deviations, a general trend in K_1 and K_3 is observed across all RBI samples and flow units (Fig. 8).

Directional statistics of the main AMS axes (Fig. 8, upper right stereograms) reveal a mean K_1 trend of 292° (α_{95} = 5.4°), while K_3 presents an average trend of 116° (α_{95} = 3.0°). AMS directional results can be used to
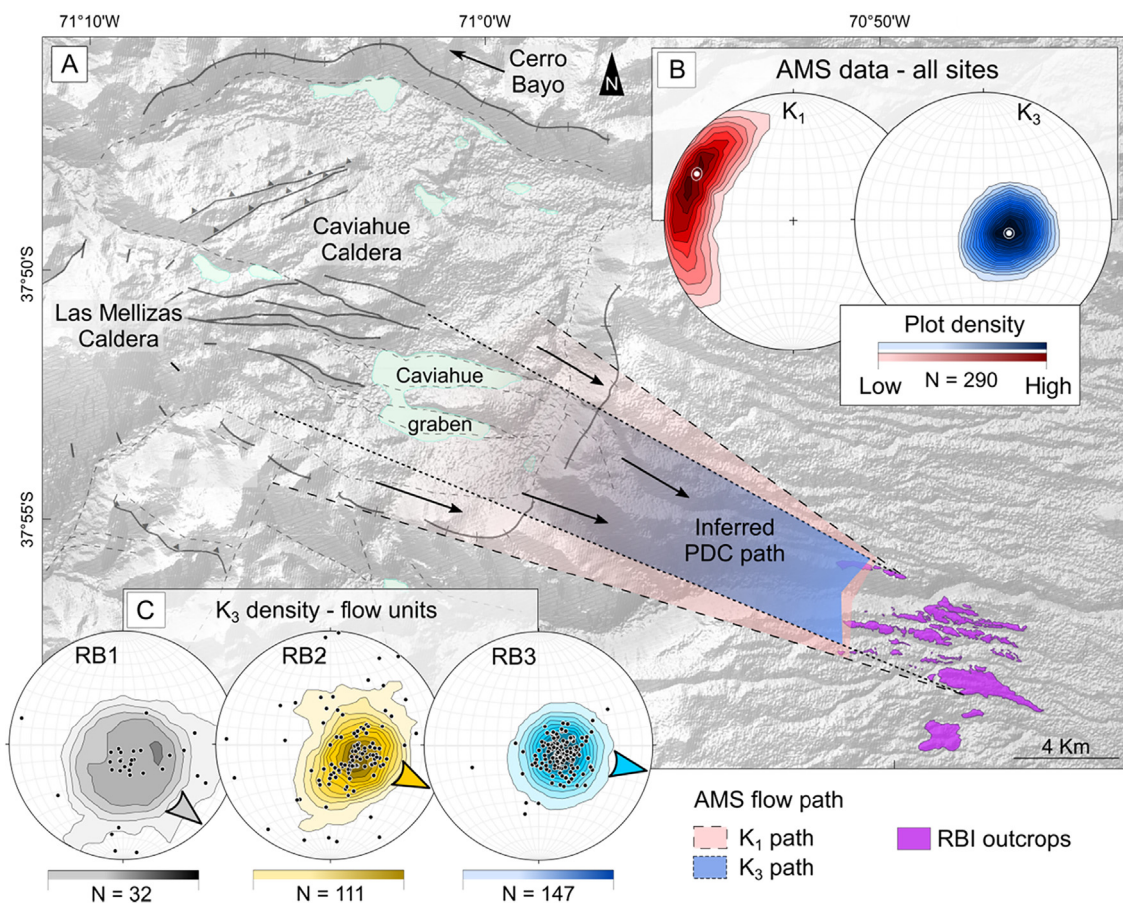
Fig. 8. Reconstruction of the PDC paths and potential source areas. A) Map of the CCVC with possible PDC paths based on both K_3 (blue) and K_1 (red) AMS measurements; source areas for RBI include the Caviahue Caldera, Las Mellizas Caldera, and Cerro Bayo dome; B) stereonets with density plots for all K_1 and K_3 measurements; C) stereonets with density plots of K_3 measurements for each RBI flow unit.

constrain possible PDC paths, considering the α_{95} as limits for the path (Fig. 8, α_{95} of K_1 in red and α_{95} of K_3 in blue). This approach indicates an emission center located in the southern segment of the Caviahue Caldera (Fig. 8). In this segment, the most prominent emission center is the Las Mellizas Caldera (Pesce, 1989; Melnick et al., 2006).

5.3. Volcanological and tectonic implications for CCVC evolution

In the past decades, several source areas were proposed for RBI ignimbrites in the literature, including: (1) the Caviahue Caldera (15 × 20 km depression in Fig. 8; Mazzoni and Licitra, 2000), (2) the Las Mellizas Caldera (Fig. 8; Pesce, 1989; Melnick et al., 2006), and (3) small dome bodies located around the Caviahue Caldera (Fig. 8; Varekamp et al., 2006). Many of these models were based mainly on field, geomorphological and geochemical data. Despite significant advances in the understanding of the CCVC evolution, these studies fail to locate the emission center of the RBI. Fig. 9A depicts a synthesis of the proposed emissions center and Fig. 9B a chart with the main geological events and volcanic deposits in the CCVC in the last 6 Ma.

One possible emission center for the RBI is the collapse of the Caviahue Caldera (Mazzoni and Licitra, 2000; Ort et al., 2014). In the sampling area the RBI radiates from the Caviahue Caldera (Fig. 9, red arrow number 1) and, as proposed by Ort et al. (2014), RBI volume could account for at least some of the collapse of the 15 × 20 Caviahue Caldera. However, the contrasting ages of the RBI and the onset of the Caviahue depression suggest that these events are most likely unrelated (Fig. 9B; Linares et al., 1999). Furthermore, a recent study by Hernando et al. (2020) in sediments of the Caviahue Graben suggests that

Caviahue Caldera was already present prior to the emplacement of the ~2.6 Ma LMVS.

Additional, small emissions centers have also been mentioned, including subvolcanic bodies such as Cerro Bayo, located to the north of the Caviahue Caldera (Fig. 9A, orange dome). However, contrasting geochemistry (Varekamp et al., 2006) and our AMS data (Fig. 9A, orange arrow number 2) do not support Cerro Bayo as a potential emission center.

Alternatively, another proposed emission center is the Las Mellizas Caldera, originally located to the west of the Caviahue Caldera (Fig. 9A, yellow depression; Pesce, 1989; Melnick et al., 2006). Despite contrasting compositions, samples from LMVS and the RBI present smooth trends in most MgO versus major elements plots, as well as compatible REE patterns (Varekamp et al., 2006). In this configuration, Las Mellizas comprises a nested caldera (Pesce, 1989). This setting implies that PDCs originating from Las Mellizas would have to either (i) surpass the ~500-m-high east wall of the Caviahue Caldera or (ii) follow a canyon to be deposited in the RBI current location (Fig. 9A, upper yellow arrow number 3).

PDCs commonly follow the general topography and especially paleovalleys (e.g., LaBerge et al., 2009; Lesti et al., 2011; Platzman et al., 2020). In this context, the canyon located in the southeastern Caviahue Caldera rim could offer a path to PDCs originated from the Las Mellizas Volcano collapse (Fig. 9A, lower yellow arrow number 3). However, our AMS data obtained at the end of this glacial valley do not support the lateral spreading of the PDC, and instead, show a rather coherent transport direction to the east-southeast (Fig. 7).

In contrast, field data and numerical simulations have shown that PDCs are capable of overrunning topographic obstacles, even in distal
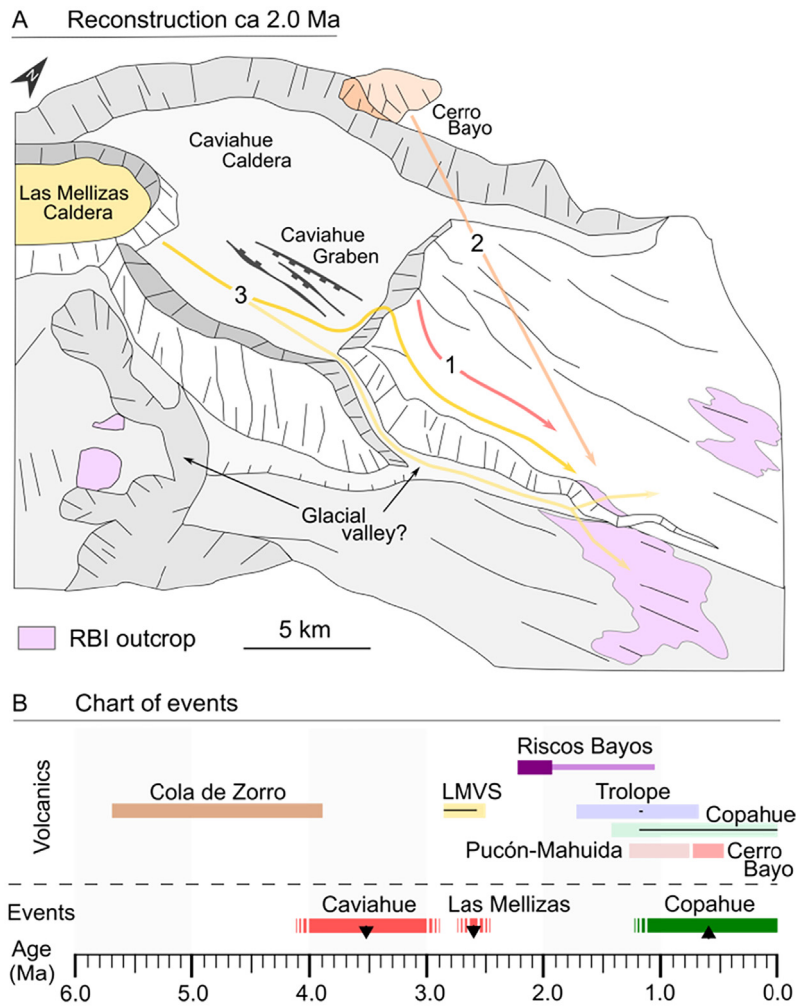
Fig. 9. Proposed source areas for RBI and main events: A) Reconstruction at ~2.0 Ma with possible PDC paths indicated by arrows: (1) Caviahue Caldera, (2) Cerro Bayo dome, and (3) Las Mellizas Caldera; B) chart of events based on the available absolute ages (Muñoz and Stern, 1988; Linares et al., 1999) and magnetic stratigraphy (Moncinhatto et al., 2019).

regions (Legros and Kelfoun, 2000; Todesco et al., 2006). The study of Todesco et al. (2006) indicates overrun of ~160 m height obstacles and suggests that topographic barriers may induce even more collapse of the eruptive column, enhancing PDC propagation. This study also indicates retention of lithic clasts at the topographic barrier followed by the deposition of more pumice-rich ignimbrites downcurrent. Legros and Kelfoun (2000) indicate the scaling of topographic barriers as high as 1500 m for Taupo pyroclastic flows. In the field, the RBI is marked by the abundance of ash and pumice fragments (which can add up to >95%), with restricted lithic-rich horizons and a massive structure, consistent with internal organization obtained in the simulations of Todesco et al. (2006). The current height of the east Caviahue Caldera wall is ~500 m. This height likely does not represent the original barrier climbed by the PDCs, as the intense glaciations and magmatism in the study region probably increased this collapse since the eruption of the RBI.

In summary, directional AMS and field data support the southern region of the Caviahue Caldera as the emission center for RBI, likely the Las Mellizas Caldera. This tectonic setting of multiple, nested emission centers and calderas is common in the Andes (e.g., Ort, 1993; Chiodi et al., 2019). Despite that, we cannot rule out the possibility of alternative emission areas located both inside and outside the Caviahue Caldera. These virtual emission centers include the Caviahue Graben (Fig. 9A) and volcanic domes originally present where the southern canyon is now located. However, geological data do not indicate the presence of

conduits, dikes, necks, or subvolcanic bodies in these regions that could have acted as emission centers for the RBI. The AMS data show clearly that the PDCs exited the Caviahue Caldera at the southeast corner and traveled downvalley from there.

5.4. Implications for PDC dynamics

In the past decades the AMS has been extensively applied to pyroclastic deposits, mainly as a tool for source area identification (e.g., Palmer and MacDonald, 1999; Hong et al., 2016; Alva-Valdivia et al., 2017). Despite that, few studies have examined how AMS relates to flow dynamics (e.g., Fisher et al., 1993; Baer et al., 1997; Ort et al., 2003, 2014; Giordano et al., 2008; LaBerge et al., 2009). In many explosive deposits, the heterogeneity of magnetic fabrics can lead to distinct interpretations, hampering the understanding of questions related to flow dynamics and emplacement of PDCs (e.g., Moncinhatto et al., 2020; Gambeta et al., 2021). The nearly homogeneous magnetic mineralogy of RBI offers the opportunity to explore these questions.

Several AMS studies show that, for non-welded pyroclastic sequences, the magnetic foliation is commonly imbricated, with both K_1 and K_3 parallel to flow direction (e.g., Fisher et al., 1993; Ort et al., 2003; Giordano et al., 2008; Cañón-Tapia and Mendoza-Borunda, 2014; Ort et al., 2014). This orientation comprises the 'parallel' magnetic fabric observed in most pyroclastic deposits (Agrò et al., 2014).
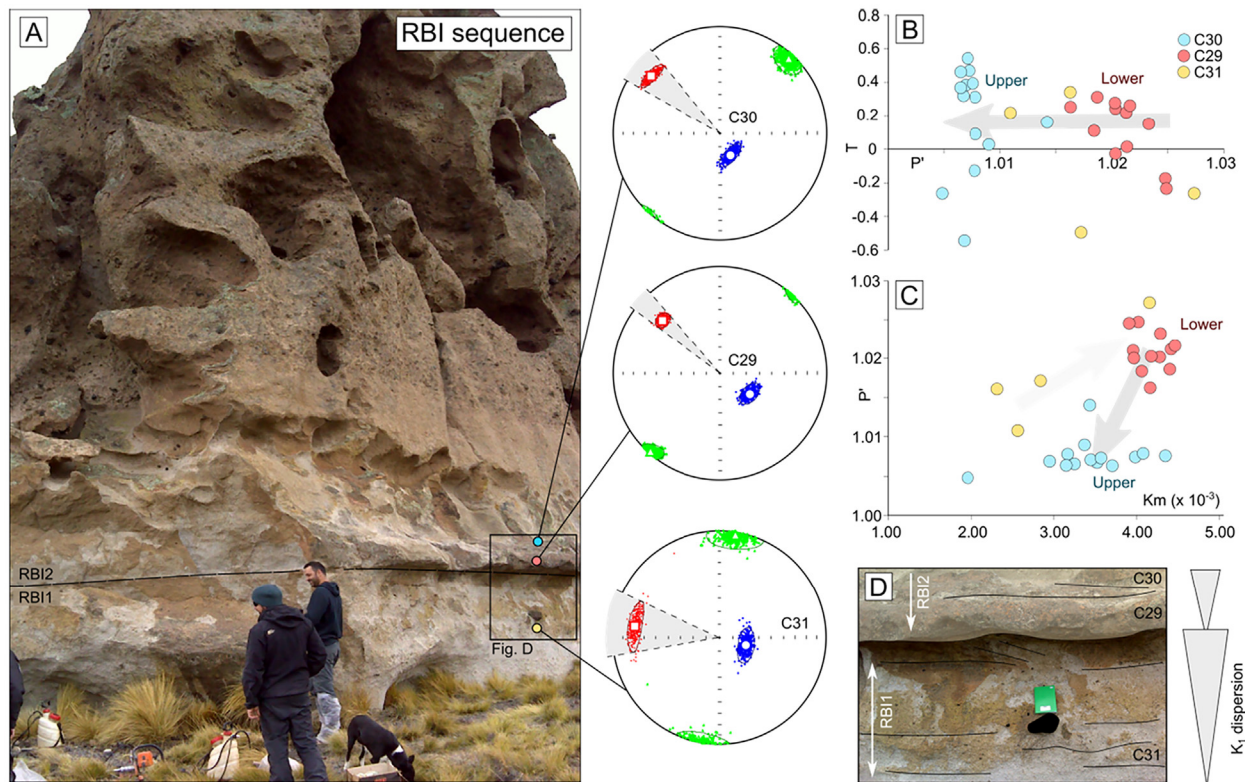
Fig. 10. Evolution of AMS fabrics and dispersion through RBI section: A) RBI flow units with stereonets; B) shape parameter and degree of anisotropy plot; C) degree of anisotropy and magnetic susceptibility plot; D) detail of the pyroclastic section and contact between upper and lower units.

However, many cases display a complex behavior (e.g., LaBerge et al., 2009; Agrò et al., 2014; Alva-Valdivia et al., 2017), expressed through 'oblique', 'transverse', and 'random' fabrics. In these cases, interpreting AMS results and extracting flow direction pose a challenge (e.g., LaBerge et al., 2009; Alva-Valdivia et al., 2017). Deviations from the parallel AMS fabrics in PDCs have been attributed to several causes, including flow dynamics (Ort et al., 1999; LaBerge et al., 2009; Agrò et al., 2014; Ort et al., 2014, 2015), and mineralogy (e.g., Rochette et al., 1992; Moncinhatto et al., 2020).

In PDCs, the flow dynamics play a significant role in the distribution and orientation of magnetic particles (Ort et al., 1999, 2014, 2015; Giordano et al., 2008). Following this reasoning, several studies have associated the orientation of AMS axes with distance from the vent and associated PDC dynamics (e.g., Fisher et al., 1993; Baer et al., 1997; Ort et al., 1999, 2003, 2015; Porreca et al., 2003). In these studies, proximal sites show overlapping, dispersed, or random K_1 and K_2 axes, while more distal portions tend to result in well-defined axes, with K_1 parallel to flow direction (Ort et al., 2014). In addition to that, in proximal regions, the orientation of K_1 may also be orthogonal to flow direction, suggesting particle rolling and the development of a transverse AMS fabric (Ort et al., 1999; Agrò et al., 2014). In the RBI, only a single site displays K_1 perpendicular to flow (C23), configuring a transverse fabric (Ort et al., 1999; Agrò et al., 2014). This site is located in the intermediate section of the RBI and as a consequence, our samples do not replicate a K_1 orientation that is dependent on the distance from the vent.

In contrast to the distance-dependent model, LaBerge et al. (2009) argue that scattering in AMS fabrics results from the gradual decrease in transport capacity of the PDC with time and changes in particle size. In this model, the upper section of a given flow unit tends to present more scatter K_1 and K_3 axes (LaBerge et al., 2009). This pattern in the magnetic fabric of increasing scatter up-section in PDC deposits has been reported only in the welded ignimbrites of the Monte Cimino

volcanic center (Italy; LaBerge et al., 2009). Here we document one of the first occurrences of this effect in non-welded PDC deposits.

In RBI sites C29, C30, and C31, AMS axis K_1 becomes progressively less constrained toward the top of each flow unit (Fig. 10A). This process also results in changes in the degree of anisotropy (Fig. 10B, C), while the basal section tends to show higher P′ values, suggesting a more effective alignment of the magnetic particles (Fig. 10B). Particles still present the same shape (T), size and similar Km values. In this model, changes of P′ and scattering of K_1 reflect changes in flow dynamics associated with a decrease in PDC transport capacity.

Báez et al. (2020b) explore the pulsating behavior of PDCs at Campo de la Piedra Pómez ignimbrite (southern Puna), mainly based on extensive field data and facies analysis. The authors suggest three eruption phases marked by waxing and waning of the PDC. In the case of homogeneous, non-welded ignimbrites, such behavior may only be detectable through the use of alternative fabric techniques such as the AMS. The results in RBI samples suggest a stratified behavior of PDCs, which may be present even in massive ignimbrites, such as the studied sequences. The origin of this behavior is associated with pulsatory mechanisms of explosive eruptions (Giordano et al., 2008; Báez et al., 2020b), which explain the distinctive flow units recorded in the RBI.

6. Conclusions

We determined the source area and emplacement dynamics of the RBI using fieldwork, AMS, and magnetic mineralogy experiments. The main results for the RBI, the CCVC, and emplacement of PDCs are:

1. The main carriers of the AMS in the RBI are titanomagnetite grains with low Ti content. The titanomagnetite occurs as sparse, primary crystals in the ash matrix.

2. AMS fabrics in RBI are predominantly oblate with K_3 imbricated and K_1 parallel to flow direction, reflecting dynamics associated with sedimentary PDC fabrics.

3. All three flow units of RBI (RB1, RB2, and RB3) present similar flow directions, with a PDC path consistent with the Las Mellizas Caldera as the emission center.

4. Despite its massive nature, AMS fabrics in the RBI reveal a decrease in transport capacity toward the top of each flow unit.

5. Loss of transport capacity results in an increase of AMS scattering and a decrease of the degree of anisotropy (P′).

Declaration of competing interest

The authors declare that all research meets the ethical guidelines, including adherence to the legal requirements. The authors also declare no conflict of interest.

Acknowledgments

Appendix A. Supplementary data

Supplementary data to this article can be found online at https://doi.org/10.1016/j.jvolgeores.2021.107283.

References

Agrò, A., Zanella, E., Le Pennec, J.-L., Temel, A., 2014. Magnetic fabric of ignimbrites: a case study from the Central Anatolian Volcanic Province. Geol. Soc. Lond., Spec. Publ. 396, 159–175. https://doi.org/10.1144/sp396.9.

Alva-Valdivia, L.M., Agarwal, A., Caballero-Miranda, C., García-Amador, B.I., Morales-Barrera, W., Rodríguez-Elizarrará, S., Rodríguez-Trejo, A., 2017. Paleomagnetic and AMS studies of the El Castillo ignimbrite, central-East Mexico: source and rock magnetic nature. J. Volcanol. Geotherm. Res. 336, 140–154. https://doi.org/10.1016/j.jvolgeores.2017.02.014.

Archanjo, C.J., Launeau, P., 2004. Magma flow inferred from preferred orientations of plagioclase of the Rio Ceará-Mirim dyke swarm (NE Brazil) and its AMS significance. Geol. Soc. Lond., Spec. Publ. 238, 285–298. https://doi.org/10.1144/gsl.sp.2004.238.01.17.

Baer, E.M., Fisher, R.V., Fuller, M., Valentine, G., 1997. Turbulent transport and deposition of the Ito pyroclastic flow: Determinations using anisotropy of magnetic susceptibility. J. Geophys. Res. 102, 22565–22586. https://doi.org/10.1029/96jb01277.

Báez, A.D., Báez, W., Caselli, A.T., Martini, M.A., Sommer, C.A., 2020a. The glaciovolcanic evolution of the Copahue volcano, Andean Southern Volcanic Zone, Argentina-Chile. J. Volcanol. Geotherm. Res. 106866. https://doi.org/10.1016/j.jvolgeores.2020.106866.

Báez, W., de Silva, S., Chiodi, A., Bustos, E., Giordano, G., Arnosio, M., Suzaño, N., Viramonte, J.G., Norini, G., Groppelli, G., 2020b. Pulsating flow dynamics of sustained, forced pyroclastic density currents: insights from a facies analysis of the Campo de la Piedra Pómez ignimbrite, southern Puna, Argentina. Bull. Volcanol. 82. https://doi.org/10.1007/s00445-020-01385-5.

Barcelona, H., Yagupsky, D., Agusto, M., 2019. The layered model of the Copahue geothermal reservoir, Argentina. Geotherm. Energy 7. https://doi.org/10.1186/s40517-019-0124-9.

Bascou, J., Camps, P., Marie Dautria, J., 2005. Magnetic versus crystallographic fabrics in a basaltic lava flow. J. Volcanol. Geotherm. Res. 145, 119–135. https://doi.org/10.1016/j.jvolgeores.2005.01.007.

Benites, S., Sommer, C.A., Lima, E.F.D., Savian, J.F., Haag, M.B., Moncinhatto, T.R., Trindade, R.I.F.D., 2020. Characterization of volcanic structures associated to the silicic magmatism of the Paraná-Etendeka Province, in the Aparados da Serra region, southern Brazil. An. Acad. Bras. Ciênc 92. https://doi.org/10.1590/0001-3765202020180981.

Cañón-Tapia, E., 2001. Factors affecting the relative importance of shape and distribution anisotropy in rocks: theory and experiments. Tectonophysics 340, 117–131. https://doi.org/10.1016/s0040-1951(01)00150-0.

Cañón-Tapia, E., Mendoza-Borunda, R., 2014. Magnetic petrofabric of igneous rocks: Lessons from pyroclastic density current deposits and obsidians. J. Volcanol. Geotherm. Res. 289, 151–169. https://doi.org/10.1016/j.jvolgeores.2014.11.006.

Cañón-Tapia, E., Walker, G.P.L., Herrero-Bervera, E., 1997. The internal structure of lava flows—insights from AMS measurements II: Hawaiian pahoehoe, toothpaste lava and "a"ā. J. Volcanol. Geotherm. Res. 76, 19–46. https://doi.org/10.1016/s0377-0273(96)00073-x.

Cas, R.A.F., Wright, J.V., 1987. Volcanic Successions Modern and Ancient. Springer Netherlands https://doi.org/10.1007/978-94-009-3167-1.

Cas, R.A.F., Wright, H.M.N., Folkes, C.B., Lesti, C., Porreca, M., Giordano, G., Viramonte, J.G., 2011. The flow dynamics of an extremely large volume pyroclastic flow, the 2.08-Ma Cerro Galán Ignimbrite, NW Argentina, and comparison with other flow types. Bull. Volcanol. 73, 1583–1609. https://doi.org/10.1007/s00445-011-0564-y.

Caselli, A.T., Liccioli, C., Tassi, F., 2016. Risk assessment and mitigation at Copahue Volcano. Active Volcanoes of the World. Springer, Berlin Heidelberg, pp. 239–254 https://doi.org/10.1007/978-3-662-48005-2_10.

Chiodi, A., Tassi, F., Báez, W., Filipovich, R., Bustos, E., Glok Galli, M., Suzaño, N., Ahumada, Ma.F., Viramonte, J.G., Giordano, G., Pecoraino, G., Vaselli, O., 2019. Preliminary conceptual model of the Cerro Blanco caldera-hosted geothermal system (Southern Puna, Argentina): Inferences from geochemical investigations. J. S. Am. Earth Sci. 94, 102213. https://doi.org/10.1016/j.jsames.2019.102213.

Constable, C., Tauxe, L., 1990. The bootstrap for magnetic susceptibility tensors. J. Geophys. Res. 95, 8383. https://doi.org/10.1029/jb095ib06p08383.

Day, R., Fuller, M., Schmidt, V.A., 1977. Hysteresis properties of titanomagnetites: Grain-size and compositional dependence. Phys. Earth Planet. Inter. 13, 260–267. https://doi.org/10.1016/0031-9201(77)90108-x.

de Silva, S.L., 1989. Altiplano-Puna volcanic complex of the Central Andes. Geol 17, 1102. https://doi.org/10.1130/0091-7613(1989)017<1102:apvcot>2.3.co;2.

Dedzo, M.G., Nédélec, A., Nono, A., Njanko, T., Font, E., Kamgang, P., Njonfang, E., Launeau, P., 2011. Magnetic fabrics of the Miocene ignimbrites from West-Cameroon: implications for pyroclastic flow source and sedimentation. J. Volcanol. Geotherm. Res. 203, 113–132. https://doi.org/10.1016/j.jvolgeores.2011.04.012.

Díaz, E.F.G., 2003. El englazamiento en la región de Caviahue-Copahue: su reinterpretación. Rev. Asoc. Geol. Argent. 58 (3), 356–366.

Dunlop, D.J., Özdemir, Ö., 1997. Rock Magnetism. Cambridge University Press https://doi.org/10.1017/cbo9780511612794.

Dunlop, D.J., Özdemir, Ö., 2015. Magnetizations in rocks and minerals. Treatise on Geophysics. Elsevier, pp. 255–308 https://doi.org/10.1016/b978-0-444-53802-4.00102-0.

Ferrari, L., López-Martínez, M., Rosas-Elguera, J., 2002. Ignimbrite flare-up and deformation in the southern Sierra Madre Occidental, western Mexico: implications for the late subduction history of the Farallon plate. Tectonics 21. https://doi.org/10.1029/2001tc001302 17-1-17–24.

Fisher, R.V., Orsi, G., Ort, M., Heiken, G., 1993. Mobility of a large-volume pyroclastic flow — emplacement of the Campanian ignimbrite, Italy. J. Volcanol. Geotherm. Res. 56, 205–220. https://doi.org/10.1016/0377-0273(93)90017-l.

Folguera, A., Rojas Vera, E., Vélez, L., Tobal, J., Orts, D., Agusto, M., Caselli, A., Ramos, V.A., 2016. A review of the geology, structural controls, and tectonic setting of Copahue volcano, Southern Volcanic Zone, Andes, Argentina. Active Volcanoes of the World. Springer, Berlin Heidelberg, pp. 3–22 https://doi.org/10.1007/978-3-662-48005-2_1.

Gambeta, J.H., Savian, J.F., Sommer, C.A., Trindade, R.I.F., 2021. Magnetic anisotropy of an ancient volcanic system: flow dynamics of post-collisional Ediacaran volcanism in southernmost Brazil. Precambrian Res. 359, 106209. https://doi.org/10.1016/j.precamres.2021.106209.

Giordano, G., Porreca, M., Musacchio, P., Mattei, M., 2008. The Holocene Secche di Lazzaro phreatomagmatic succession (Stromboli, Italy): evidence of pyroclastic density current origin deduced by facies analysis and AMS flow directions. Bull. Volcanol. 70, 1221–1236. https://doi.org/10.1007/s00445-008-0198-x.

Graham, J.W., 1954. Magnetic susceptibility anisotropy, an unexploited petrofabric element. Geol. Soc. Am. Bull. 65, 1257–1258.

Haag, M., Moncinhatto, T., Sommer, C., Savian, J., Caselli, A., Trindade, R., Hartmann, G., Poletti, W., 2020. Source area and emplacement conditions of Riscos Bayos Ignimbrites, Caviahue-Copahue Volcanic Complex (Argentina). EGU General Assembly. 2020. https://doi.org/10.5194/egusphere-egu2020-2704.

Haag, M.B., de Freitas, R.B., Sommer, C.A., Savian, J.F., Lima, E.F., Gambeta, J.H., da Lyra, D.S., da Trindade, R.I.F., 2021. Multi-proxy case study of a Neoproterozoic rhyolite flow in southernmost Brazil: emplacement mechanisms and implications for ancient felsic lavas. J. S. Am. Earth Sci. 107, 102982. https://doi.org/10.1016/j.jsames.2020.102982.

Hargraves, R.B., Johnson, D., Chan, C.Y., 1991. Distribution anisotropy: the cause of AMS in igneous rocks? Geophys. Res. Lett. 18, 2193–2196. https://doi.org/10.1029/91gl01777.

Harrison, R.J., Feinberg, J.M., 2008. FORCinel: an improved algorithm for calculating first-order reversal curve distributions using locally weighted regression smoothing. Geochem. Geophys. Geosyst. 9. https://doi.org/10.1029/2008gc001987.

Hernando, I.R., Bucher, J., del Papa, C.E., Eisermann, J.O., Göllner, P.L., Guzmán, S.R., Balbis, C., Petrinovic, I.A., 2020. Unraveling the timing of the Caviahue depression, Andean Southern Volcanic Zone: insights from the sedimentary infill. Int. J. Earth Sci. (Geol Rundsch) https://doi.org/10.1007/s00531-020-01936-3.

Heslop, D., Dekkers, M.J., Kruiver, P.P., Van Oorschot, I.H.M., 2002. Analysis of isothermal remanent magnetization acquisition curves using the expectation-maximization algorithm. Geophys. J. Int. 148, 58–64. https://doi.org/10.1046/j.0956-540x.2001.01558.x.

Hildreth, W., Moorbath, S., 1988. Crustal contributions to arc magmatism in the Andes of Central Chile. Contrib. Mineral. Petrol. 98, 455–489. https://doi.org/10.1007/bf00372365.

Hong, H., Yu, Y., Doh, S.-J., Suk, D., Kim, J., 2016. Magnetic fabrics and source implications of Chisulryoung Ignimbrites, South Korea. Front. Earth Sci. 4. https://doi.org/10.3389/feart.2016.00079.

Hrouda, F., 1982. Magnetic anisotropy of rocks and its application in geology and geophysics. Geophys. Surv. 5, 37–82. https://doi.org/10.1007/bf01450244.

Hrouda, F., 2003. Stud. Geophys. Geod. 47, 847–861. https://doi.org/10.1023/a:1026398920172.

Jelinek, V., 1981. Characterization of the magnetic fabric of rocks. Tectonophysics 79, T63–T67. https://doi.org/10.1016/0040-1951(81)90110-4.

Kruiver, P.P., Passier, H.F., 2001. Coercivity analysis of magnetic phases in sapropel S1 related to variations in redox conditions, including an investigation of theSratio. Geochem. Geophys. Geosyst. 2. https://doi.org/10.1029/2001gc000181.

LaBerge, R.D., Porreca, M., Mattei, M., Giordano, G., Cas, R.A.F., 2009. Meandering flow of a pyroclastic density current documented by the anisotropy of magnetic susceptibility (AMS) in the quartz latite ignimbrite of the Pleistocene Monte Cimino volcanic Centre (Central Italy). Tectonophysics 466, 64–78. https://doi.org/10.1016/j.tecto.2008.09.009.

Lattard, D., Engelmann, R., Kontny, A., Sauerzapf, U., 2006. Curie temperatures of synthetic titanomagnetites in the Fe-Ti-O system: effects of composition, crystal chemistry, and thermomagnetic methods. J. Geophys. Res. 111. https://doi.org/10.1029/2006jb004591.

Legros, F., Kelfoun, K., 2000. On the ability of pyroclastic flows to scale topographic obstacles. J. Volcanol. Geotherm. Res. 98, 235–241. https://doi.org/10.1016/s0377-0273(99)00184-5.

Lesti, C., Porreca, M., Giordano, G., Mattei, M., Cas, R.A.F., Wright, H.M.N., Folkes, C.B., Viramonte, J., 2011. High-temperature emplacement of the Cerro Galán and Toconquis Group ignimbrites (Puna plateau, NW Argentina) determined by TRM analyses. Bull. Volcanol. 73, 1535–1565. https://doi.org/10.1007/s00445-011-0536-2.

Linares, E., Ostera, H.A., Mas, L., 1999. Cronologia potasio-argon del complejo efusivo Copahue-Caviahue, Provincia del Neuquen. Rev. Asoc. Geol. Argentina 54 (3), 240–247.

Magee, C., Stevenson, C., O'Driscoll, B., Schofield, N., McDermott, K., 2012. An alternative emplacement model for the classic Ardnamurchan cone sheet swarm, NW Scotland, involving lateral magma supply via regional dykes. J. Struct. Geol. 43, 73–91. https://doi.org/10.1016/j.jsg.2012.08.004.

Maxbauer, D.P., Feinberg, J.M., Fox, D.L., 2016. MAX UnMix: a web application for unmixing magnetic coercivity distributions. Comput. Geosci. 95, 140–145. https://doi.org/10.1016/j.cageo.2016.07.009.

Mazzoni, M.M., Licitra, D., 2000. Significado estratigráfico y volcanológico de ignimbritas neógenas con composición intermedia en la zona del lago Caviahue, Neuquén. Rev. Asoc. Geol. Argent. 55 (3), 188–200.

Melnick, D., Folguera, A., Ramos, V.A., 2006. Structural control on arc volcanism: the Caviahue–Copahue complex, Central to Patagonian Andes transition (38°S). J. S. Am. Earth Sci. 22, 66–88. https://doi.org/10.1016/j.jsames.2006.08.008.

Moncinhatto, T.R., Oliveira, W.P., Haag, M.B., Hartmann, G.A., Savian, J.F., Poletti, W., Sommer, C.A., Caselli, A.T., Trindade, R.I.F., 2019. Paleosecular variaton from Northern Patagonia recorded by 0–5 Ma Caviahue-Copahue lava flows. Sixth Biennial Meeting of Latinmag, Rancagua. Latinmag Letters. Rancagua. 9, pp. 1–7.

Moncinhatto, T.R., Haag, M.B., Hartmann, G.A., Savian, J.F., Poletti, W., Sommer, C.A., Caselli, A.T., Trindade, R.I.F., 2020. Mineralogical control on the magnetic anisotropy of lavas and ignimbrites: a case study in the Caviahue-Copahue field (Argentina). Geophys. J. Int. 220, 821–838. https://doi.org/10.1093/gji/ggz483.

Morgan, L.A., Doherty, D.J., Leeman, W.P., 1984. Ignimbrites of the Eastern Snake River Plain: evidence for major caldera-forming eruptions. J. Geophys. Res. 89, 8665. https://doi.org/10.1029/jb089ib10p08665.

Muñoz, J.B., Stern, C.R., 1988. The quaternary volcanic belt of the southern continental margin of South America: transverse structural and petrochemical variations across the segment between 38S and 39S. J. S. Am. Earth Sci. 1 (2), 147–161. https://doi.org/10.1016/0895-9811(88)90032-6.

Ort, M.H., 1993. Eruptive processes and caldera formation in a nested downsagcollapse caldera: Cerro Panizos, Central Andes Mountains. J. Volcanol. Geotherm. Res. 56, 221–252. https://doi.org/10.1016/0377-0273(93)90018-m.

Ort, M.H., Rosi, M., Anderson, C.D., 1999. Correlation of deposits and vent locations of the proximal Campanian Ignimbrite deposits, Campi Flegrei, Italy, based on natural remanent magnetization and anisotropy of magnetic susceptibility characteristics. J. Volcanol. Geotherm. Res. 91, 167–178. https://doi.org/10.1016/s0377-0273(99)00034-7.

Ort, M.H., Orsi, G., Pappalardo, L, Fisher, R.V., 2003. Anisotropy of magnetic susceptibility studies of depositional processes in the Campanian Ignimbrite, Italy. Bull. Volcanol. 65, 55–72. https://doi.org/10.1007/s00445-002-0241-2.

Ort, M.H., Newkirk, T.T., Vilas, J.F., Vazquez, J.A., 2014. Towards the definition of AMS facies in the deposits of pyroclastic density currents. Geol. Soc. Lond., Spec. Publ. 396, 205–226. https://doi.org/10.1144/sp396.8.

Ort, M.H., Porreca, M., Geissman, J.W., 2015. The use of palaeomagnetism and rock magnetism to understand volcanic processes: introduction. Geol. Soc. Lond., Spec. Publ. 396, 1–11. https://doi.org/10.1144/sp396.17.

Palmer, H.C., MacDonald, W.D., 1999. Anisotropy of magnetic susceptibility in relation to source vents of ignimbrites: empirical observations. Tectonophysics 307, 207–218. https://doi.org/10.1016/s0040-1951(99)00126-2.

Pasqualon, N.G., Savian, J.F., Lima, E.F., Luz, F.R., Moncinhatto, T.R., Trindade, R.I.F., 2020. Emplacement dynamics of alkaline volcanic and subvolcanic rocks in Trindade Island, Brazil. J. Volcanol. Geotherm. Res. 406, 107078. https://doi.org/10.1016/j.jvolgeores.2020.107078.

Pesce, A., 1989. Evolución volcano-tectónica del complejo efusivo Copahue– Caviahue y su modelo geotérmico preliminar. Rev. Asoc. Geol. Argent. 44, 307–327.

Platzman, E.S., Sparks, R.S.J., Cooper, F.J., 2020. Fabrics, facies, and flow through a large-volume ignimbrite: Pampa De Oxaya, Chile. Bull. Volcanol. 82. https://doi.org/10.1007/s00445-019-1345-2.

Porreca, M., Mattei, M., Giordano, G., De Rita, D., Funiciello, R., 2003. Magnetic fabric and implications for pyroclastic flow and lahar emplacement, Albano maar, Italy. J. Geophys. Res. 108. https://doi.org/10.1029/2002jb002102.

Roberts, A.P., Cui, Y., Verosub, K.L., 1995. Wasp-waisted hysteresis loops: mineral magnetic characteristics and discrimination of components in mixed magnetic systems. J. Geophys. Res. 100, 17909–17924. https://doi.org/10.1029/95jb00672.

Roberts, A.P., Pike, C.R., Verosub, K.L., 2000. First-order reversal curve diagrams: a new tool for characterizing the magnetic properties of natural samples. J. Geophys. Res. 105, 28461–28475. https://doi.org/10.1029/2000jb900326.

Roberts, A.P., Almeida, T.P., Church, N.S., Harrison, R.J., Heslop, D., Li, Y., Li, J., Muxworthy, A.R., Williams, W., Zhao, X., 2017. Resolving the origin of pseudo-single domain magnetic behavior. J. Geophys. Res. Solid Earth 122, 9534–9558. https://doi.org/10.1002/2017jb014860.

Roberts, A.P., Tauxe, L., Heslop, D., Zhao, X., Jiang, Z., 2018. A critical appraisal of the "day" diagram. J. Geophys. Res. Solid Earth 123, 2618–2644. https://doi.org/10.1002/2017jb015247.

Robertson, D.J., France, D.E., 1994. Discrimination of remanence-carrying minerals in mixtures, using isothermal remanent magnetization acquisition curves. Phys. Earth Planet. Inter. 82, 223–234.

Rochette, P., Jackson, M., Aubourg, C., 1992. Rock magnetism and the interpretation of anisotropy of magnetic susceptibility. Rev. Geophys. 30, 209. https://doi.org/10.1029/92rg00733.

Schindelin, J., Arganda-Carreras, I., Frise, E., Kaynig, V., Longair, M., Pietzsch, T., Preibisch, S., Rueden, C., Saalfeld, S., Schmid, B., Tinevez, J.-Y., White, D.J., Hartenstein, V., Eliceiri, K., Tomancak, P., Cardona, A., 2012. Fiji: an open-source platform for biological-image analysis. Nat. Methods 9, 676–682. https://doi.org/10.1038/nmeth.2019.

Sielfeld, G., Cembrano, J., Lara, L., 2017. Transtension driving volcano-edifice anatomy: Insights from Andean transverse-to-the-orogen tectonic domains. Quat. Int. 438, 33–49. https://doi.org/10.1016/j.quaint.2016.01.002.

Sommer, C.A., Haag, M.B., Caselli, A.T., 2016. Determinação numérica de parâmetros reológicos para sistemas vulcânicos de diferentes composições e idades. X Simpósio Sul-Brasileiro de Geologia, Curitiba. Boletim de Resumos do X Simpósio Sul-Brasileiro de Geologia. Curitiba: SBG/UFPR 2017. v. 10.

Sparks, R.S.J., 1976. Grain size variations in ignimbrites and implications for the transport of pyroclastic flows. Sedimentology 23, 147–188. https://doi.org/10.1111/j.1365-3091.1976.tb00045.x.

Stern, C.R., 2004. Active Andean volcanism: its geologic and tectonic setting. Rev. Geol. Chile 31. https://doi.org/10.4067/s0716-02082004000200001.

Syono, Y., 1960. Magnetic susceptibility of some rock forming silicate minerals such as amphiboles, biotites, cordierites and garnets. J. Geomagn. Geoelectr. 11, 85–93. https://doi.org/10.5636/jgg.11.85.

Tarling, D.H., Hrouda, F., 1993. The Magnetic Anisotropy of Rocks. Chapman & Hall, London https://doi.org/10.1002/gj.3350300111 217p.

Tassi, F., Vaselli, O., Caselli, A.T. (Eds.), 2016. Copahue Volcano, Active Volcanoes of the World. Springer Berlin Heidelberg https://doi.org/10.1007/978-3-662-48005-2.

Tauxe, L., Kylstra, N., Constable, C., 1991. Bootstrap statistics for paleomagnetic data. J. Geophys. Res. 96, 11723. https://doi.org/10.1029/91jb00572.

Tauxe, L., Banerjee, S.K., Butler, R.F., Van Der Voo, R., 2018. Essentials of Paleomagnetism, 5th Web Edition.

Todesco, M., Neri, A., Esposti Ongaro, T., Papale, P., Rosi, M., 2006. Pyroclastic flow dynamics and hazard in a caldera setting: application to Phlegrean Fields (Italy). Geochem. Geophys. Geosyst. 7. https://doi.org/10.1029/2006gc001314 n/a-n/a.

Varekamp, J.C., deMoor, J.M., Merrill, M.D., Colvin, A.S., Goss, A.R., Vroon, P.Z., Hilton, D.R., 2006. Geochemistry and isotopic characteristics of the Caviahue-Copahue volcanic complex, Province of Neuquén, Argentina. Evolution of an Andean Margin: A Tectonic and Magmatic View from the Andes to the Neuquén Basin (35°-39°S Lat). Geological Society of America https://doi.org/10.1130/2006.2407(15.

Velez, M.L., Euillades, P., Caselli, A., Blanco, M., Díaz, J.M., 2011. Deformation of Copahue volcano: Inversion of InSAR data using a genetic algorithm. J. Volcanol. Geotherm. Res. 202, 117–126. https://doi.org/10.1016/j.jvolgeores.2011.01.012.